NURBS-based finite element analysis of functionally graded plates: static bending, vibration, buckling and flutter

Navid Valizadeh[a,1], Sundararajan Natarajan[b,2,*], Octavio A Gonzalez-Estrada[c,3], Timon Rabczuk[a,4], Tinh Quoc Bui[d,5], Stéphane PA Bordas[c,6]

[a]*Institute of Structural Mechanics, Bauhaus-Universität Weimar, Marienstraße, Weimar*
[b]*School of Civil and Environmental Engineering, The University of New South Wales, Sydney, Australia*
[c]*Institute of Mechanics and Advanced Materials, Cardiff University, Cardiff, UK*
[d]*Chair of Structural Mechanics, Department of Civil Engineering, University of Siegen, Siegen, Germany*

Abstract

In this paper, a non-uniform rational B-spline based iso-geometric finite element method is used to study the static and dynamic characteristics of functionally graded material (FGM) plates. The material properties are assumed to be graded only in the thickness direction and the effective properties are computed either using the rule of mixtures or by Mori-Tanaka homogenization scheme. The plate kinematics is based on the first order shear deformation plate theory (FSDT). The shear correction factors are evaluated employing the energy equivalence principle and a simple modification to the shear correction factor is presented to alleviate shear locking. Static bending, mechanical and thermal buckling, linear free flexural vibration and supersonic flutter analysis of FGM plates are numerically studied. The accuracy of the present formulation is validated against available three-dimensional solutions. A detailed numerical study is carried out to examine the influence of the gradient index, the plate aspect ratio and the plate thickness on the global response of functionally graded material plates.

*Corresponding author
[1]navid.valizadeh@uni-weimar.de
[2]sundararajan.natarajan@gmail.com
[3]agestrada@gmail.com
[4]timon.rabczuk@uni-weimar.de
[5]bui-quoc@bauwesen.uni-siegen.de
[6]stephane.bordas@alum.northwestern.edu

1. Introduction

Since its introduction to decrease the thermal stresses in propulsion systems and in airframes for space application [1], functionally graded materials (FGMs) have led researchers to investigate the structural behaviour of such structures. FGMs are considered to be an alternative for certain class of aerospace structures exposed to high temperature environment. FGMs are characterized by a smooth transition from one material to another, thus circumventing high inter-laminar shear stresses and de-lamination that persists in laminated composites. Thus, for structural integrity, FGMs have advantages over the fiber-matrix composites.

1.1. Background

The investigation of the static and the dynamic behaviour of FGM structures is fairly well covered in the literature. Some of the important contributions are discussed here. Different plate theories, viz, FSDT [2, 3, 4], second and other higher order accurate theory [5, 6, 7] have been used to describe plate kinematics. Existing approaches in the literature to study plate and shell structures made up of FGMs uses finite element method based on Lagrange basis functions [2, 8, 4], meshfree methods [5, 6]. All existing approaches show shear locking when applied to thin plates. Different techniques by which the locking phenomenon can be suppressed include:

- Retain the original interpolations and subsequently use an optimal integration rule for evaluating the bending and the shear terms;

- Mixed interpolation technique [9];

- Use field redistributed substitute shape functions [10, 11];

- Discrete shear gap method [12];

2

- Stabilized conforming nodal integration [13], i.e., strain smoothing, SFEM [14, 15].

- Use p-adaptivity, for example Moving Least Square approximations [16].

He *et al.,* [17] presented a finite element formulation based on thin plate theory for the vibration control of FGM plates with integrated piezoelectric sensors and actuators under mechanical load, whereas Liew *et al.,* [18] have analyzed the active vibration control of plates subjected to a thermal gradient using shear deformation theory. The parametric resonance of FGM plates is discussed in [19] by Ng *et al.,* based on Hamilton's principle and the assumed mode technique. Yang and Shen [20, 3] have analyzed the dynamic response of thin FGM plates subjected to impulsive loads using a Galerkin Procedure coupled with modal superposition methods, whereas, by neglecting the heat conduction effect, such plates and panels in thermal environments have been examined based on shear deformation with temperature dependent material properties [3]. The static deformation and vibration of FGM plates based on higher-order shear deformation theory is studied by Qian *et al.,* [5] using the meshless local Petrov-Galerkin method (MLPG) and Natarajan and Ganapathi [7] using shear flexible elements. Matsunaga [21] presented analytical solutions for simply supported rectangular FGM plates based on second-order shear deformation theory, whereas, three dimensional solutions are proposed in [22, 23] for vibrations of simply supported rectangular FGM plates. Reddy [2] presented finite element solutions for the dynamic analysis of FGM plates and Ferreira *et al.,* [6] performed dynamic analysis of FGM plates based on higher order shear and normal deformable plate theory using MLPG. Birman [24] and Javaheri and Eslami [25] have studied buckling of FGM plates subjected to in-plane compressive loading. Woo *et al.,* [26] analyzed the thermo-mechanical postbuckling behaviour of plates and shallow cylindrical FGM panels using a classical theory. Ganapathi *et al.,* [8], using a $\mathcal{C}^o$ shear flexible quadrilateral element, studied buckling of non-rectangular FGM plates under mechanical and thermal loads. Prakash and Ganapathi [27] studied the linear flutter characteristics of FGM panels exposed to supersonic flow. Haddadpour *et al.,* [28] and Sohn and Kim [29, 30] investigated the nonlinear aspects of flutter characteristics using the finite element method. FGM plates, like other plate structures, may develop flaws. Recently, Yang and Chen [31] and Kitipornchai *et al.,* [32] studied the dynamic characteristics

of FGM beams with an edge crack. Natarajan *et al.,* [33, 34] and Baiz *et al.,* [35] studied the influence of the crack length on the free flexural vibrations of FGM plates using the XFEM and smoothed XFEM, respectively.

1.2. Approach

The main objective of this paper is to investigate the potential of NURBS based iso-geometric finite element methods to study the static and dynamic characteristics of Reissner-Mindlin plates. The present formulation also suffers from shear locking when lower order NURBS functions are used as basis functions. da Vaiga *et al.,* [36] showed that the shear locking phenomena can be suppressed by using higher order NURBS functions. A similar approach was employed to suppress shear locking in the element-free Galerkin method [37]. In this paper, we propose a simple technique to suppress shear locking, which relies on the introduction of an artificial shear correction factor [38] when lower order NURBS basis functions are used. The drawback of this approach is that the shear correction factor is problem dependent.

1.3. Outline

The paper is organized as follows. A brief overview on functionally graded materials and Reissner-Mindlin plate theory is presented in the next section. Section 3 presents an overview of NURBS basis functions and a simple correction to the shear terms to alleviate shear locking. The efficiency of the present formulation, numerical results and parametric studies are presented in Section 5, followed by concluding remarks in the last section.

2. Theoretical Formulation

2.1. Functionally graded material

A rectangular plate made of a mixture of ceramic and metal ~~is considered~~ with the coordinates x, y along the in-plane directions and z along the thickness direction (see Figure (1)). The material on the top surface $(z = h/2)$ of the plate is ceramic rich and is graded to metal at the bottom surface of the plate $(z = -h/2)$ by a power

law distribution. The effective properties of the FGM plate can be computed by using the rule of mixtures or by employing the Mori-Tanaka homogenization scheme.

Let $V_i(i = c, m)$ be the volume fraction of the phase material. The subscripts c and m refer to ceramic and metal phases, respectively. The volume fraction of ceramic and metal phases are related by $V_c + V_m = 1$ and V_c is expressed as:

$$V_c(z) = \left(\frac{2z + h}{2h}\right)^n \tag{1}$$

where n is the volume fraction exponent ($n \geq 0$), also known as the gradient index. The variation of the composition of ceramic and metal is linear for $n = 1$, the value of $n = 0$ represents a fully ceramic plate and any other value of n yields a composite material with a smooth transition from ceramic to metal.

Rule of mixtures

Based on the rule of mixtures, the effective property of a FGM is computed using the following expression:

$$P = P_c V_c + P_m V_m \tag{2}$$

Mori-Tanaka homogenization method

Based on the Mori-Tanaka homogenization method, the effective Young's modulus and Poisson's ratio are computed from the effective bulk modulus K and the effective shear modulus G as [4]

$$
\begin{aligned}
\frac{K_{\text{eff}} - K_m}{K_c - K_m} &= \frac{V_c}{1 + V_m \frac{3(K_c - K_m)}{3K_m + 4G_m}} \\
\frac{G_{\text{eff}} - G_m}{G_c - G_m} &= \frac{V_c}{1 + V_m \frac{(G_c - G_m)}{(G_m + f_1)}}
\end{aligned}
\tag{3}
$$

where

$$f_1 = \frac{G_m(9K_m + 8G_m)}{6(K_m + 2G_m)} \tag{4}$$

The effective Young's modulus E_{eff} and Poisson's ratio ν_{eff} can be computed from the following relations:

$$E_{\text{eff}} = \frac{9K_{\text{eff}}G_{\text{eff}}}{3K_{\text{eff}} + G_{\text{eff}}}$$
$$\nu_{\text{eff}} = \frac{3K_{\text{eff}} - 2G_{\text{eff}}}{2(3K_{\text{eff}} + G_{\text{eff}})} \tag{5}$$

The effective mass density ρ is computed using the rule of mixtures. The effective heat conductivity κ_{eff} and the coefficient of thermal expansion α_{eff} is given by:

$$\frac{\kappa_{\text{eff}} - \kappa_m}{\kappa_c - \kappa_m} = \frac{V_c}{1 + V_m \frac{(\kappa_c - \kappa_m)}{3\kappa_m}}$$
$$\frac{\alpha_{\text{eff}} - \alpha_m}{\alpha_c - \alpha_m} = \frac{\left(\frac{1}{K_{\text{eff}}} - \frac{1}{K_m}\right)}{\left(\frac{1}{K_c} - \frac{1}{K_m}\right)} \tag{6}$$

Temperature distribution through the thickness

The temperature variation is assumed to occur in the thickness direction only and the temperature field is considered to be constant in the xy-plane. In such a case, the temperature distribution along the thickness can be obtained by solving a steady state heat transfer problem:

$$-\frac{d}{dz}\left[\kappa(z)\frac{dT}{dz}\right] = 0, \quad T = T_c \text{ at } z = h/2; \quad T = T_m \text{ at } z = -h/2 \tag{7}$$

6

The solution of Equation (7) is obtained by means of a polynomial series [39] as

$$T(z) = T_m + (T_c - T_m)\eta(z, h) \tag{8}$$

where,

$$
\begin{aligned}
\eta(z, h) = \frac{1}{C} &\left[\left(\frac{2z+h}{2h} \right) - \frac{\kappa_{cm}}{(n+1)\kappa_m} \left(\frac{2z+h}{2h} \right)^{n+1} + \right. \\
&\frac{\kappa_{cm}^2}{(2n+1)\kappa_m^2} \left(\frac{2z+h}{2h} \right)^{2n+1} - \frac{\kappa_{cm}^3}{(3n+1)\kappa_m^3} \left(\frac{2z+h}{2h} \right)^{3n+1} \\
&\left. + \frac{\kappa_{cm}^4}{(4n+1)\kappa_m^4} \left(\frac{2z+h}{2h} \right)^{4n+1} - \frac{\kappa_{cm}^5}{(5n+1)\kappa_m^5} \left(\frac{2z+h}{2h} \right)^{5n+1} \right];
\end{aligned}
\tag{9}
$$

$$
\begin{aligned}
C = 1 &- \frac{\kappa_{cm}}{(n+1)\kappa_m} + \frac{\kappa_{cm}^2}{(2n+1)\kappa_m^2} - \frac{\kappa_{cm}^3}{(3n+1)\kappa_m^3} \\
&+ \frac{\kappa_{cm}^4}{(4n+1)\kappa_m^4} - \frac{\kappa_{cm}^5}{(5n+1)\kappa_m^5}
\end{aligned}
\tag{10}
$$

2.2. Reissner-Mindlin Plates

The displacements u, v, w at a point (x, y, z) in the plate (see Figure (1)) from the medium surface are expressed as functions of the mid-plane displacements u_o, v_o, w_o and independent rotations θ_x, θ_y of the normal in yz and xz planes, respectively, as:

$$
\begin{aligned}
u(x, y, z, t) &= u_o(x, y, t) + z\theta_x(x, y, t) \\
v(x, y, z, t) &= v_o(x, y, t) + z\theta_y(x, y, t) \\
w(x, y, z, t) &= w_o(x, y, t)
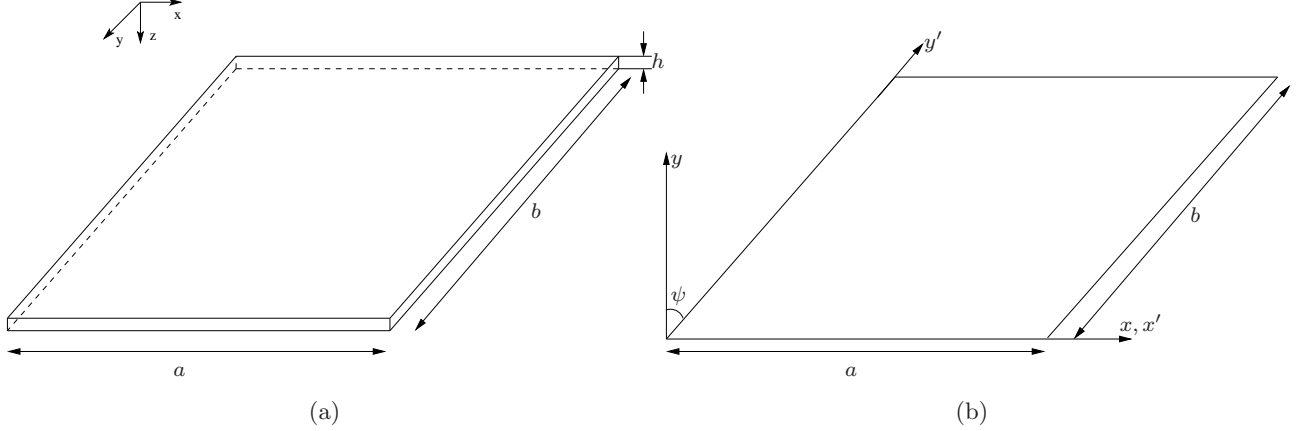\end{aligned}
\tag{11}
$$

where t is the time.

Figure 1: (a) coordinate system of a rectangular FGM plate, (b) Coordinate system of a skew plate

The strains in terms of mid-plane deformation can be written as:

$$\boldsymbol{\varepsilon} = \left\{ \begin{array}{c} \boldsymbol{\varepsilon}_p \\ 0 \end{array} \right\} + \left\{ \begin{array}{c} z\boldsymbol{\varepsilon}_b \\ \boldsymbol{\varepsilon}_s \end{array} \right\} \tag{12}$$

The midplane strains $\boldsymbol{\varepsilon}_p$, bending strain $\boldsymbol{\varepsilon}_b$, shear strain $\boldsymbol{\varepsilon}_s$ in Equation (12) are written as:

$$\boldsymbol{\varepsilon}_p = \left\{ \begin{array}{c} u_{o,x} \\ v_{o,y} \\ u_{o,y} + v_{o,x} \end{array} \right\}, \qquad \boldsymbol{\varepsilon}_b = \left\{ \begin{array}{c} \theta_{x,x} \\ \theta_{y,y} \\ \theta_{x,y} + \theta_{y,x} \end{array} \right\},$$

$$\boldsymbol{\varepsilon}_s = \left\{ \begin{array}{c} \theta_x + w_{o,x} \\ \theta_y + w_{o,y} \end{array} \right\}. \tag{13}$$

where the subscript 'comma' represents the partial derivative with respect to the spatial coordinate succeeding

it. The membrane stress resultants $\mathbf{N}$ and the bending stress resultants $\mathbf{M}$ can be related to the membrane strains, ε_p and bending strains ε_b through the following constitutive relations:

$$\mathbf{N} = \left\{ \begin{array}{c} N_{xx} \\ N_{yy} \\ N_{xy} \end{array} \right\} = \mathbf{A}\varepsilon_p + \mathbf{B}\varepsilon_b$$

$$\mathbf{M} = \left\{ \begin{array}{c} M_{xx} \\ M_{yy} \\ M_{xy} \end{array} \right\} = \mathbf{B}\varepsilon_p + \mathbf{D_b}\varepsilon_b \tag{14}$$

where the matrices $\mathbf{A} = A_{ij}, \mathbf{B} = B_{ij}$ and $\mathbf{D_b} = D_{ij}; (i,j = 1,2,6)$ are the extensional, bending-extensional coupling and bending stiffness coefficients and are defined as:

$$\{A_{ij}, \ B_{ij}, \ D_{ij}\} = \int_{-h/2}^{h/2} \overline{Q}_{ij} \left\{1, \ z, \ z^2\right\} \ dz \tag{15}$$

Similarly, the transverse shear force $Q = \{Q_{xz}, Q_{yz}\}$ is related to the transverse shear strains ε_s through the following equation:

$$Q_{ij} = E_{ij}\varepsilon_s \tag{16}$$

where $E_{ij} = \int_{-h/2}^{h/2} \overline{Q}v_i v_j \ dz; \ (i,j = 4,5)$ is the transverse shear stiffness coefficient, v_i, v_j is the transverse shear coefficient for non-uniform shear strain distribution through the plate thickness. The stiffness coefficients $\overline{Q}_{ij}$ are defined as:

9

$$\overline{Q}_{11} = \overline{Q}_{22} = \frac{E(z)}{1 - \nu^2}; \qquad \overline{Q}_{12} = \frac{\nu E(z)}{1 - \nu^2}; \qquad \overline{Q}_{16} = \overline{Q}_{26} = 0$$
$$\overline{Q}_{44} = \overline{Q}_{55} = \overline{Q}_{66} = \frac{E(z)}{2(1 + \nu)} \tag{17}$$

where the modulus of elasticity $E(z)$ and Poisson's ratio ν are given by Equation (5). The thermal stress resultant $\mathbf{N}^{\text{th}}$ and the moment resultant $\mathbf{M}^{\text{th}}$ are:

$$\mathbf{N}^{\text{th}} = \left\{ \begin{array}{c} N_{xx}^{\text{th}} \\ N_{yy}^{\text{th}} \\ N_{xy}^{\text{th}} \end{array} \right\} = \int\limits_{-h/2}^{h/2} \overline{Q}_{ij} \alpha(z, T) \left\{ \begin{array}{c} 1 \\ 1 \\ 0 \end{array} \right\} \Delta T(z) \, \mathrm{d}z$$

$$\mathbf{M}^{\text{th}} = \left\{ \begin{array}{c} M_{xx}^{\text{th}} \\ M_{yy}^{\text{th}} \\ M_{xy}^{\text{th}} \end{array} \right\} = \int\limits_{-h/2}^{h/2} \overline{Q}_{ij} \alpha(z, T) \left\{ \begin{array}{c} 1 \\ 1 \\ 0 \end{array} \right\} \Delta T(z) \, z \, \mathrm{d}z$$

$$\tag{18}$$

where the ~~thermal~~ coefficient of expansion $\alpha(z, T)$ is given by Equation (6) and $\Delta T(z) = T(z) - T_o$ is the temperature rise from the reference temperature and T_o is the temperature at which there are no thermal strains. The strain energy function U is given by:

$$U(\boldsymbol{\delta}) = \frac{1}{2} \int_{\Omega} \left\{ \boldsymbol{\varepsilon}_p^{\mathrm{T}} \mathbf{A} \boldsymbol{\varepsilon}_p + \boldsymbol{\varepsilon}_p^{\mathrm{T}} \mathbf{B} \boldsymbol{\varepsilon}_b + \boldsymbol{\varepsilon}_b^{\mathrm{T}} \mathbf{B} \boldsymbol{\varepsilon}_p + \boldsymbol{\varepsilon}_b^{\mathrm{T}} \mathbf{D} \boldsymbol{\varepsilon}_b + \boldsymbol{\varepsilon}_s^{\mathrm{T}} \mathbf{E} \boldsymbol{\varepsilon}_s \right\} \, \mathrm{d}\Omega \tag{19}$$

where $\boldsymbol{\delta} = \{u, v, w, \theta_x, \theta_y\}$ is the vector of the degree of freedom associated to the displacement field in a finite element discretization. Following the procedure given in [40], the strain energy function U given in Equation

(19) can be rewritten as:

$$U(\boldsymbol{\delta}) = \frac{1}{2}\boldsymbol{\delta}^{\mathrm{T}}\mathbf{K}\boldsymbol{\delta} \tag{20}$$

where $\mathbf{K}$ is the linear stiffness matrix. The kinetic energy of the plate is given by:

$$T(\boldsymbol{\delta}) = \frac{1}{2}\int_{\Omega}\left\{p(\dot{u}_o^2 + \dot{v}_o^2 + \dot{w}_o^2) + I(\dot{\theta}_x^2 + \dot{\theta}_y^2)\right\}\ \mathrm{d}\Omega \tag{21}$$

where $p = \int_{-h/2}^{h/2}\rho(z)\ dz$, $I = \int_{-h/2}^{h/2}z^2\rho(z)\ dz$ and $\rho(z)$ is the mass density that varies through the thickness of the plate. When the plate is subjected to a temperature field, this in turn results in in-plane stress resultants, $\mathbf{N}^{\mathrm{th}}$. The external work due to the in-plane stress resultants developed in the plate under a thermal load is given by:

$$V(\boldsymbol{\delta}) = \int_{\Omega}\left\{\frac{1}{2}\left[N_{xx}^{\mathrm{th}}w_{,x}^2 + N_{yy}^{\mathrm{th}}w_{,y}^2 + 2N_{xy}^{\mathrm{th}}w_{,x}w_{,y}\right] + \frac{h^2}{24}\left[N_{xx}^{\mathrm{th}}\left(\theta_{x,x}^2 + \theta_{y,x}^2\right) + N_{yy}^2\left(\theta_{x,y}^2 + \theta_{y,y}^2\right) + 2N_{xy}^{\mathrm{th}}\left(\theta_{x,x}\theta_{x,y} + \theta_{y,x}\theta_{y,y}\right)\right]\right\}\ d\Omega \tag{22}$$

The governing equations of motion are obtained by writing the Lagrange equations of motion given by:

$$\frac{d}{dt}\left[\frac{\partial(T-U)}{\partial\dot{\boldsymbol{\delta}}_i}\right] - \left[\frac{\partial(T-U)}{\partial\boldsymbol{\delta}_i}\right] = 0, \quad i = 1, 2, \cdots, n \tag{23}$$

The governing equations obtained using the minimization of total potential energy are solved using Galerkin finite element method. The finite element equations thus derived are:

Static bending:

$$\left(\mathbf{K} + \mathbf{K}_G\right)\boldsymbol{\delta} = \mathbf{F} \tag{24}$$

Free vibration:

$$\mathbf{M}\ddot{\boldsymbol{\delta}} + (\mathbf{K} + \mathbf{K}_G)\,\boldsymbol{\delta} = \mathbf{0} \tag{25}$$

Buckling analysis:

Mechanical Buckling.

$$(\mathbf{K} + \lambda\mathbf{K}_G)\,\boldsymbol{\delta} = \mathbf{0} \tag{26}$$

Thermal Buckling.

$$(\mathbf{K} + \Delta T\mathbf{K}_G)\,\boldsymbol{\delta} = \mathbf{0} \tag{27}$$

where $\boldsymbol{\delta}$ is the vector of degree of freedom associated to the displacement field in a finite element discretization, $\Delta T (= T_c - T_m)$ is the critical temperature difference, λ is the critical buckling load and $\mathbf{K}$, $\mathbf{K}_G$ are the linear stiffness and geometric stiffness matrices, respectively. The critical temperature difference is computed using a standard eigenvalue algorithm.

Flutter analysis: The work done by the applied non-conservative loads is:

$$W(\boldsymbol{\delta}) = \int_\Omega \Delta p w \, \mathrm{d}\Omega \tag{28}$$

where Δp is the aerodynamic pressure. The aerodynamic pressure based on first-order, high Mach number approximation to linear potential flow is given by:

$$\Delta p = \frac{\rho_a U_a^2}{\sqrt{M_\infty^2 - 1}} \left[\frac{\partial w}{\partial x} \cos\theta' + \frac{\partial w}{\partial y} \sin\theta' + \left(\frac{1}{U_a}\right) \frac{M_\infty^2 - 2}{M_\infty^2 - 1} \frac{\partial w}{\partial t} \right] \tag{29}$$

where ρ_a, U_a, M_∞ and θ' are the free stream air density, velocity of air, Mach number and flow angle, respectively.

The static aerodynamic approximation for Mach numbers between $\sqrt{2}$ and 2 is [41]:

$$\Delta p = \frac{\rho_a U_a^2}{\sqrt{M_\infty^2 - 1}} \left[\frac{\partial w}{\partial x} \cos \theta' + \frac{\partial w}{\partial y} \sin \theta' \right] \tag{30}$$

Substituting Equation (20) - (28) in Lagrange's equations of motion, the following governing equation is obtained:

$$\mathbf{M}\ddot{\boldsymbol{\delta}} + (\mathbf{K} + \lambda\overline{\mathbf{A}})\boldsymbol{\delta} = \mathbf{0} \tag{31}$$

After substituting the characteristic of the time function [42] $\ddot{\boldsymbol{\delta}} = -\omega^2 \boldsymbol{\delta}$, the following algebraic equation is obtained:

$$\left[(\mathbf{K} + \lambda\overline{\mathbf{A}}) - \omega^2 \mathbf{M} \right] \boldsymbol{\delta} = \mathbf{0} \tag{32}$$

where $\mathbf{K}$ is the stiffness matrix, $\mathbf{M}$ is the consistent mass matrix, $\lambda = \frac{\rho_a U_a^2}{\sqrt{M_\infty^2 - 1}}$, $\overline{\mathbf{A}}$ is the aerodynamic force matrix and ω is the natural frequency. When $\lambda = 0$, the eigenvalue of ω is real and positive, since the stiffness matrix and mass matrix are symmetric and positive definite. However, the aerodynamic matrix $\overline{\mathbf{A}}$ is unsymmetric and hence complex eigenvalues ω are expected for $\lambda > 0$. As λ increases monotonically from zero, two of these eigenvalues will approach each other and become complex conjugates. In this study, λ_{cr} is considered to be the value of λ at which the first coalescence occurs.

3. Non-Uniform Rational B-Splines

In this study, the finite element approximation uses NURBS basis function. We give here only a brief introduction to NURBS. More details on their use in FEM are given in [43, 44]. The key ingredients in the construction of NURBS basis functions are: the knot vector (a non decreasing sequence of parameter values, $\xi_i \leq \xi_{i+1}, i = 0, 1, \cdots, m-1$), the control points, P_i, the degree of the curve p and the weight associated to a control point, w. The ith B-spline basis function of degree p, denoted by $N_{i,p}$ is defined as:

13

$$N_{i,0}(\xi) = \begin{cases} 1 & \text{if } \xi_i \leq \xi \leq \xi_{i+1} \\ 0 & \text{else} \end{cases}$$

$$N_{i,p}(\xi) = \frac{\xi - \xi_i}{\xi_{i+p} - \xi_i} N_{i,p-1}(\xi) + \frac{\xi_{i+p+1} - \xi}{\xi_{i+p+1} - \xi_{i+1}} N_{i+1,p-1}(\xi) \tag{33}$$

A pth degree NURBS curve is defined as follows:

$$\mathbf{C}(\xi) = \frac{\displaystyle\sum_{i=0}^{m} N_{i,p}(\xi) w_i \mathbf{P}_i}{\displaystyle\sum_{i=0}^{m} N_{i,p}(\xi) w_i} \tag{34}$$
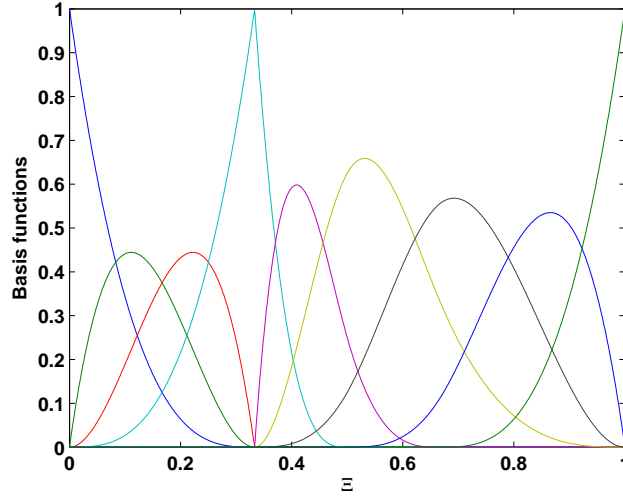
Figure 2: non-uniform rational B-splines, order of the curve = 3

where $\mathbf{P}_i$ are the control points and w_i are the associated weights. Figure (2) shows the third order non-uniform rational B-splines for a knot vector, $\Xi = \{0, 0, 0, 0, 1/3, 1/3, 1/3, 1/2, 2/3, 1, 1, 1, 1\}$. NURBS basis functions has the following properties: (i) non-negativity, (ii) partition of unity, $\sum_i N_{i,p} = 1$; (iii) interpolatory

14

at the end points. As the same function is also used to represent the geometry, the exact representation of the geometry is preserved. It should be noted that the continuity of the NURBS functions can be tailored to the needs of the problem. The B-spline surfaces are defined by the tensor product of basis functions in two parametric dimensions ξ and η with two knot vectors, one in each dimension as:

$$\mathbf{C}(\xi, \eta) = \sum_{i=1}^{n} \sum_{j=1}^{m} N_{i,p}(\xi) M_{j,q}(\eta) \mathbf{P}_{i,j} \tag{35}$$

where $\mathbf{P}_{i,j}$ is the bidirectional control net and $N_{i,p}$ and $M_{j,q}$ are the B-spline basis functions defined on the knot vectors over an $m \times n$ net of control points $\mathbf{P}_{i,j}$. The NURBS surface is then defined by:

$$\mathbf{C}(\xi, \eta) = \frac{\sum_{i=1}^{n} \sum_{j=1}^{m} N_{i,p}(\xi) M_{j,q}(\eta) \mathbf{P}_{i,j} w_i w_j}{w(\xi, \eta)} \tag{36}$$

where $w(\xi, \eta)$ is the weighting function. The displacement field within the control mesh is approximated by:

$$\{u_o^e, v_o^e, w_o^e, \theta_x^e, \theta_y^e\} = \mathbf{C}(\xi, \eta)\{u_{oJ}, v_{oJ}, w_{oJ}, \theta_{xJ}, \theta_{yJ}\}, \tag{37}$$

where $u_{oJ}, v_{oJ}, w_{oJ}, \theta_{xJ}, \theta_{yJ}$ are the nodal variables and $\mathbf{C}(\xi, \eta)$ are the basis functions given by Equation (36).

4. Shear Locking

Transverse shear deformations are included in the formulation of Mindlin theory for thick plates. In Mindlin theory, the transverse normal to the mid surface of the plate before deformation remain straight but not necessarily normal to the mid surface after deformation. This relaxed the continuity requirement on the assumed displacement fields. But as the plate becomes very thin, care must be taken in not to violate the following relationship

$$\nabla w + \theta = 0 \tag{38}$$

15

i.e., the shear strain ε_s must vanish in the domain as the thickness approaches zero.

Artificial shear correction factor

Lower order NURBS basis functions, like any other function, suffer from shear locking when applied to thin plates. Kikuchi and Ishii [38] introduced an artificial shear correction factor to suppress shear locking in 4-noded quadrilateral element. In this paper, we employ the same technique to suppress the shear locking syndrome in lower order NURBS basis functions. The modified shear correction factor is given by:

$$
\upsilon_e = \upsilon \frac{\left(\frac{h}{\beta l_e}\right)^2}{\left(1 + \left(\frac{h}{\beta l_e}\right)^{2n}\right)^{1/n}}
\tag{39}
$$

where n, β are positive integers, l_e is the diameter of the element (=maximum or diagonal length of the element), h is thickness of the element and υ is the shear correction factor. Here, the shear correction factor obtained based on energy equivalence principle as outlined in [45, 33] is used.

5. Numerical Examples

In this section, we present the static bending response, free vibration, buckling and flutter analysis of FGM plates using a NURBS based finite element method. The effect of various parameters, viz., material gradient index n, skewness of the plate ψ, the plate aspect ratio a/b, the plate thickness a/h and boundary conditions on the global response is numerically studied. The top surface of the plate is ceramic rich and the bottom surface of the plate is metal rich. The material properties used for the FGM components are listed in Table 1.

Skew boundary transformation

For skew plates supported on two adjacent edges, the edges of the boundary elements may not be parallel to the global axes (x, y, z). In order to specify the boundary conditions on skew edges, it is necessary to use the edge displacements (u'_o, v'_o, w'_o), etc., in a local coordinate system (x', y', z') (see Figure (1)). The element

Table 1: Material properties.

Property	Aluminum	Zirconia	Zirconia	Alumina
	Al	ZrO_2-1	ZrO_2-2	Al_2O_3
E (GPa)	70	200	151	380
ν	0.3	0.3	0.3	0.3
κ W/mK	204	2.09	2.09	10.4
$\alpha/^\circ$C	23×10^{-6}	10×10^{-6}	10×10^{-6}	7.2×10^{-6}
ρ kg/m^3	2707	5700	3000	3800

matrices corresponding to the skew edges are transformed from global axes to local axes on which the boundary conditions can be conveniently specified. The relation between the global and local degrees of a particular node can be obtained through the following transformation [33]

$$\boldsymbol{\delta} = \mathbf{L}_g \boldsymbol{\delta}'$$
(40)

where $\boldsymbol{\delta}$ and $\boldsymbol{\delta}'$ are the generalized displacement vector in the global and the local coordinate system, respectively. The nodal transformation matrix for a node I on the skew boundary is given by

$$\mathbf{L}_g = \begin{bmatrix} \cos\psi & \sin\psi & 0 & 0 & 0 \\ -\sin\psi & \cos\psi & 0 & 0 & 0 \\ 0 & 0 & 1 & 0 & 0 \\ 0 & 0 & 0 & \cos\psi & \sin\psi \\ 0 & 0 & 0 & -\sin\psi & \cos\psi \end{bmatrix}$$
(41)

where ψ defines the skewness of the plate.

5.1. Static Bending

Let us consider a Al/ZrO$_2$ FGM square plate with length-to-thickness $a/h = 5$, subjected to a uniform load with fully simply supported (SSSS) and fully clamped (CCCC) boundary conditions. Four different values for the gradient index ($n = 0, 0.5, 1, 2$) are considered in this study. The plate is modelled with 4, 8, 16, 24 and 32 control points per side. Tables 2 and 3 summarize the IGA results with quadratic, cubic and quartic NURBS elements for SSSS and CCCC boundary conditions. It can be seen that for all polynomial orders, the convergence of the results is quite fast. For cubic and quartic NURBS elements, the convergence is almost achieved with 16 control points per side. Table 4 compares the results from the present formulation with other approaches available in the literature [46, 47, 48] and a very good agreement can be observed.

Next, we illustrate the performance of the present isogeometric method for thin plate problems. A simply supported and a clamped Al/ZrO$_2$-1 square plates subjected to uniform load are considered, while the length-to-thickness (a/h) varies from 5 to 10^6 and the gradient index ranges from 0 to 2. Two individual approaches are employed: one applied the stabilization technique to eliminate shear locking named S-IGA and the other one, normal IGA, without considering any specific technique for shear locking. The plate is modelled using quadratic NURBS elements with 13×13 control points. The normalized center deflection $\overline{w}_c = 100w_c\frac{E_ch^3}{12(1-\nu^2)pa^4}$ and the normalized axial stress $\overline{\sigma}_{xx} = \sigma_{xx}\frac{h^2}{pa^2}$ at the top surface of the center of the plate for SSSS and CCCC boundary conditions are depicted in Figures 3 - 4, respectively. It is observed that IGA results are subjected to shear locking when the plate becomes thin ($a/h > 100$). However, the S-IGA results are almost independent of the length-to-thickness ratio for thin plates. The same observations also reported in [49] for laminated composite plates. The results using the S-IGA agree very well with those given in [48] using the NS-DSG3 element.

FGM plates under thermo-mechanical loads

Here, the present isogeometric method is verified on FGM plates subjected to thermo-mechanical loads. A simply supported Al/ZrO$_2$ plate with aluminium at the bottom surface and zirconia at the top surface is considered. The plate with length $a = 0.2$ m and thickness h=0.01 m is modelled employing quadratic NURBS elements. For

Table 2: The normalized center deflection for fully simply supported Al/ZrO$_2$-1 FGM square plate with $a/h = 5$, subjected to a uniformly distributed load p using IGA. *At least 5 control points per side are needed for 1 quartic NURBS element.

Method	Number of Control Points	gradient index, n			
		0	0.5	1	2
Quadratic	4	0.162098	0.218914	0.256018	0.293806
	8	0.171617	0.232392	0.271879	0.311459
	16	0.171649	0.232439	0.271935	0.311520
	24	0.171651	0.232441	0.271938	0.311523
	32	0.171651	0.232442	0.271938	0.311523
Cubic	4	0.163329	0.220598	0.257991	0.296053
	8	0.171658	0.232452	0.271950	0.311536
	16	0.171651	0.232441	0.271938	0.311522
	24	0.171651	0.232442	0.271938	0.311523
	32	0.171651	0.232442	0.271938	0.311523
Quartic	5*	0.172910	0.234167	0.273959	0.313821
	8	0.171690	0.232495	0.272000	0.311594
	16	0.171651	0.232442	0.271938	0.311523
	24	0.171651	0.232442	0.271938	0.311523
	32	0.171651	0.232442	0.271938	0.311523

Table 3: The normalized center deflection for fully clamped Al/ZrO$_2$-1 FGM square plate with $a/h = 5$, subjected to a uniformly distributed load p using IGA. *At least 5 control points per side are needed for 1 quartic NURBS element.

Method	Number of	gradient index, n			
	Control Points	0	0.5	1	2
Quadratic	4	0.052510	0.06818	0.079306	0.093421
	8	0.075831	0.101036	0.117946	0.136557
	16	0.076017	0.101305	0.118264	0.136905
	24	0.076024	0.101315	0.118276	0.136918
	32	0.076025	0.101316	0.118278	0.136920
Cubic	4	0.056337	0.07342	0.085447	0.100403
	8	0.076031	0.101324	0.118287	0.136931
	16	0.076025	0.101316	0.118277	0.136921
	24	0.076025	0.101317	0.118278	0.136921
	32	0.076026	0.101317	0.118279	0.136921
Quartic	5*	0.077690	0.103620	0.120980	0.139973
	8	0.076092	0.101409	0.118387	0.137043
	16	0.076026	0.101317	0.118279	0.136921
	24	0.076026	0.101317	0.118279	0.136921
	32	0.076026	0.101317	0.118279	0.136921

Table 4: The normalized center deflection for fully clamped Al/ZrO$_2$-1 FGM square plate with $a/h = 5$, subjected to a uniformly distributed load p using 13 $\times$13 control points for various boundary conditions. *At least 5 control points per side are needed for 1 quartic NURBS element.

Method	Number of Control Points	gradient index, n			
		0	0.5	1	2
SSSS	IGA-Quadratic	0.1717	0.2324	0.2719	0.3115
	IGA-Cubic	0.1717	0.2324	0.2719	0.3115
	IGA-Quartic	0.1717	0.2324	0.2719	0.3115
	NS-DSG3 [48]	0.1721	0.2326	0.2716	0.3107
	ES-DSG3 [48]	0.1700	0.2296	0.2680	0.3066
	MITC4 [48]	0.1715	0.2317	0.2704	0.3093
	$kp-$Ritz [47]	0.1722	0.2403	0.2811	0.3221
	MLPG [46]	0.1671	0.2505	0.2905	0.3280
CCCC	IGA-Quadratic	0.0760	0.1013	0.1183	0.1369
	IGA-Cubic	0.0760	0.1014	0.1183	0.1369
	IGA-Quartic	0.0760	0.1014	0.1183	0.1369
	NS-DSG3 [48]	0.0788	0.1051	0.1227	0.1420
	ES-DSG3 [48]	0.0761	0.1013	0.1183	0.1370
	MITC4 [48]	0.0758	0.1010	0.1179	0.1365
	$kp-$Ritz [47]	0.0774	0.1034	0.1207	0.1404
	MLPG [46]	0.0731	0.1073	0.1253	0.1444
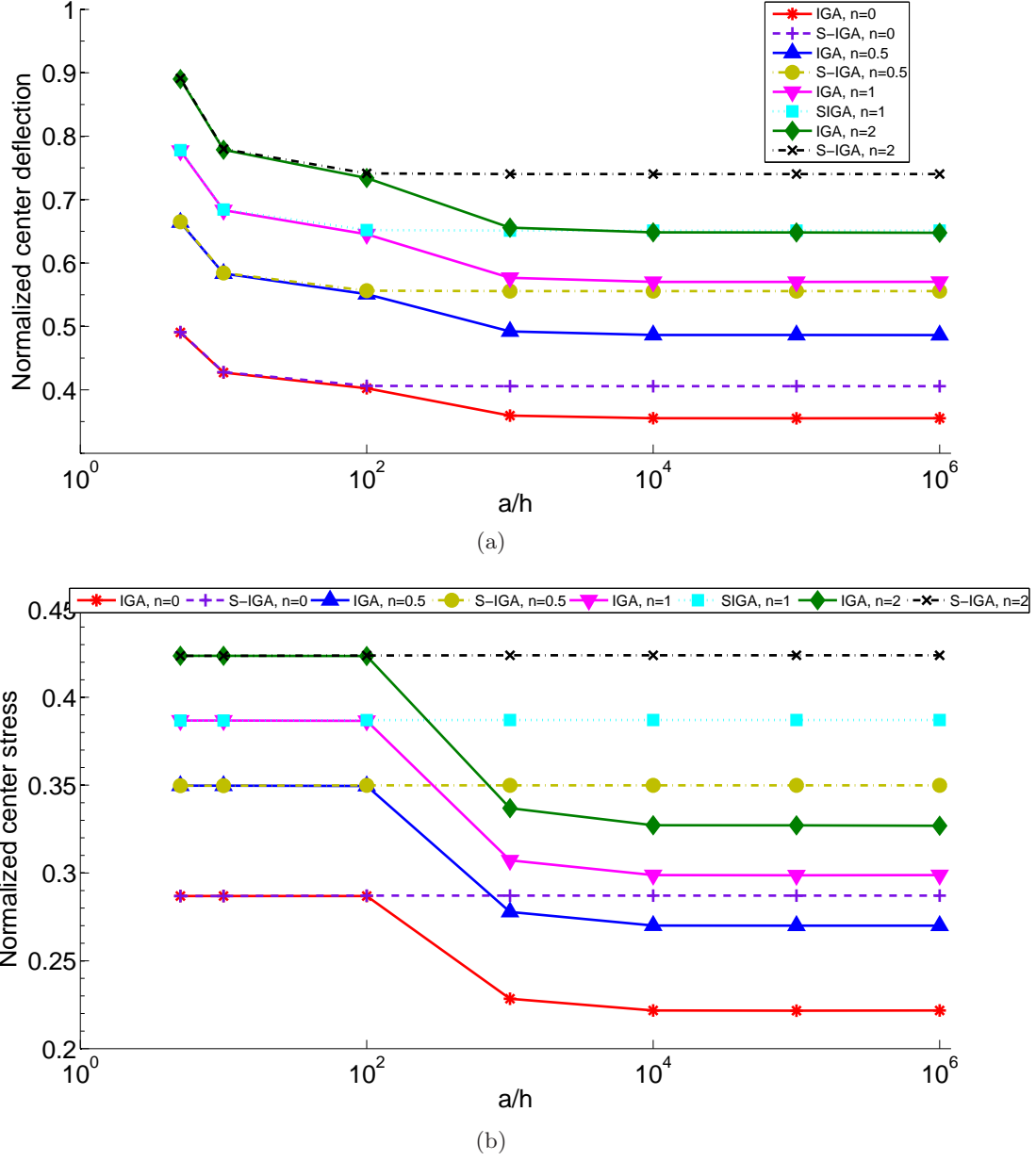
Figure 3: The normalized center deflection, $\overline{w}_c$ and the normalized axial stress $\overline{\sigma}_{xx}$ as a function of a/h for a simply supported Al/Zr0$_2$-1 FGM square plate subjected to a uniform load, p: (a) normalized center deflection and (b) normalized center stress.

(a)

(b)
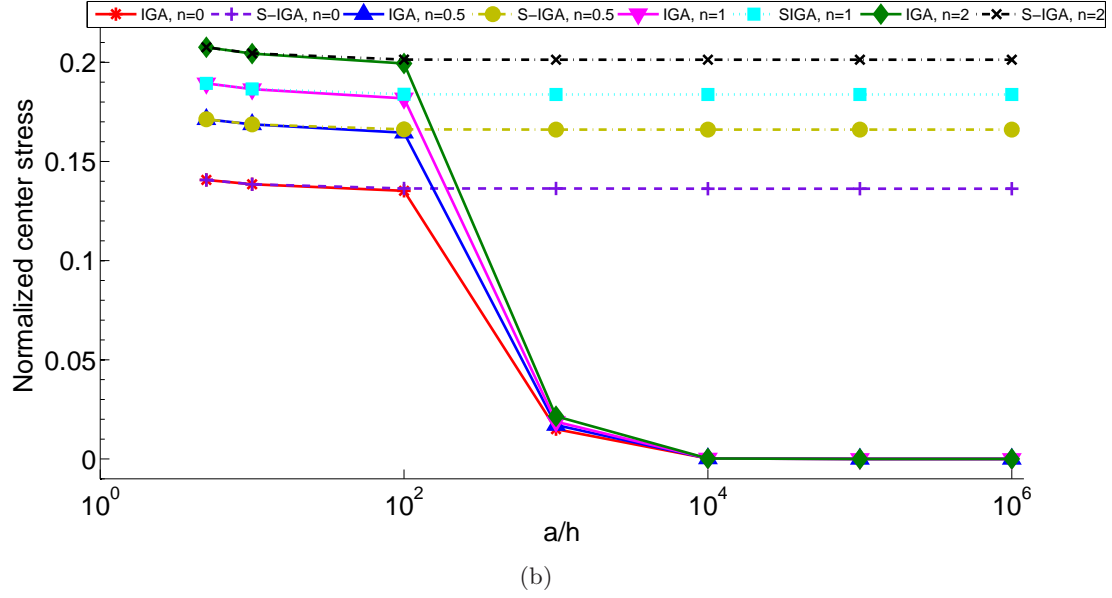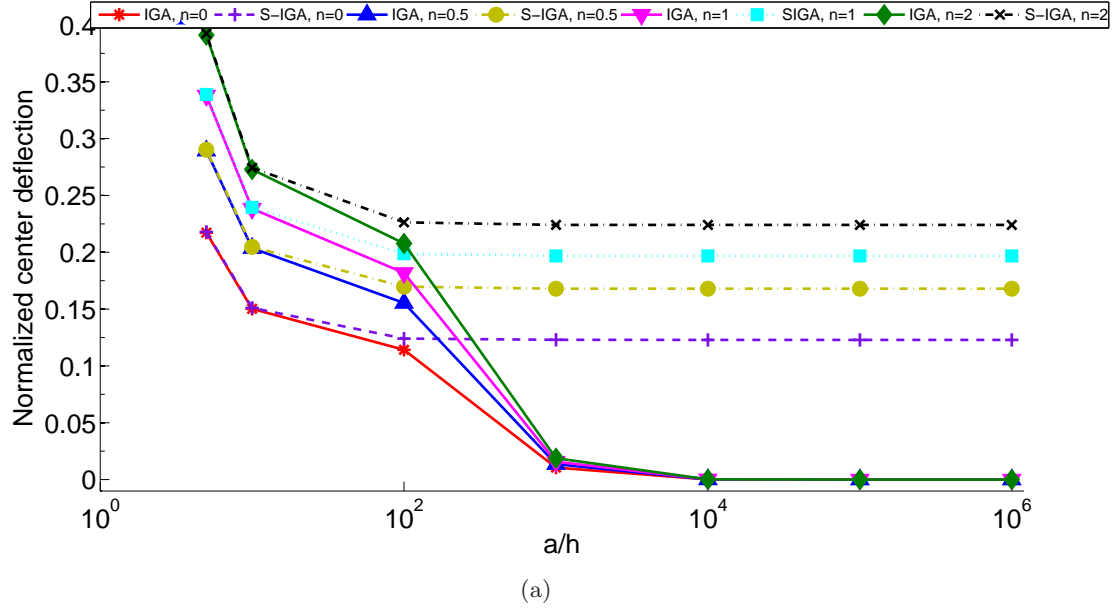
Figure 4: The normalized center deflection, $\overline{w}_c$ and the normalized axial stress $\overline{\sigma}_{xx}$ as a function of a/h for a clamped Al/Zr0$_2$-1 FGM square plate subjected to a uniform load, p: (a) normalized center deflection and (b) normalized center stress.

23

comparison, a mesh with 13 control points per side is used. At first, we study the behaviour of SSSS Al/ZrO$_2$-I FGM plate under a uniform mechanical load. Figure (5) shows the distributions of the normalized axial stress through the thickness of the plate computed for different values of the gradient index n. The results are in excellent agreement with those given in [46, 48]. Figure (6) plots the central deflection $\overline{w}_c = 100 w_c \frac{E_c h^3}{12(1-\nu^2)pa^4}$ of the plate with respect to various load parameters, $\overline{p} = pa^4/(E_m h^4)$, given in the interval [-14, 0] for different values of the gradient index n. It can be seen that the central deflection of the plate linearly increases with respect to the load. It is also observed that the central deflection increases with the gradient index k. As expected, the metallic plate has the largest deflection, while the ceramic plate has the lowest. Note that the results match well with those given in [48, 50]. Figure (6) shows the normalized axial stress at points on the vertical line passing through the centroid of simply supported Al/ZrO$_2$-2 FGM square plate subjected to a uniform mechanical load p. The results agree well with the results reported in [47, 48]. It is observed that for isotropic plates ($i.e, n = 0$) the axial stress distribution is linear while it is nonlinear for FGM plates. For FGM plates, the magnitude of the axial stress at the bottom is less than the one at the top. The maximum compressive stress at the top surface of the plate has been obtained for the FGM plate with $n = 2$, whilst the metallic only or ceramic only plates has the ~~minimum~~ tensile stress at the bottom surface.

FGM plates subjected to thermal loading

Next, we study the behaviour of FGM plates under the thermal loading. A Al/ZrO$_2$-2 FGM plate with length $a = 0.2$m and thickness $h = 0.01$m is considered. The temperature at the top surface of the plate is varied from $0°$C to $500°$C, while the temperature at the bottom surface is maintained at $20°$C. The temperature of the stress free state is assumed to be at $T_o = 0°$C. Figure (7) depicts the non-dimensional center deflection of the plate under the thermal load. This problem was solved by Zhao and Liew, using the element free kp-Ritz method [51] and by Xuan *et al.,* [48] using NS-DSG3 elements. The results obtained with our IGA method agree very well with those given in [51, 48]. From Figure (7), it is observed that the metal plate gives the maximum deflection because of its high thermal conductivity. The deflection of the FGM plate with the gradient index
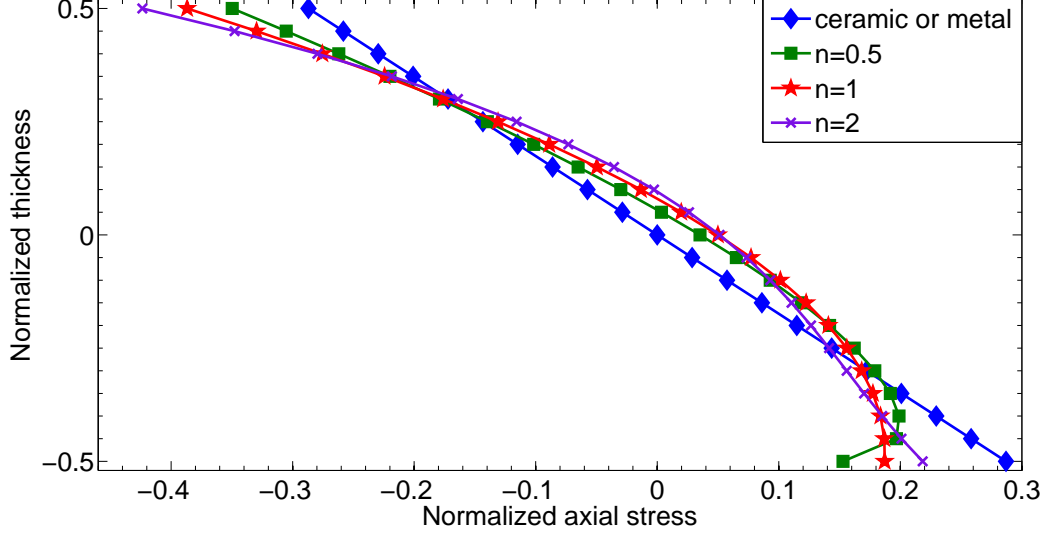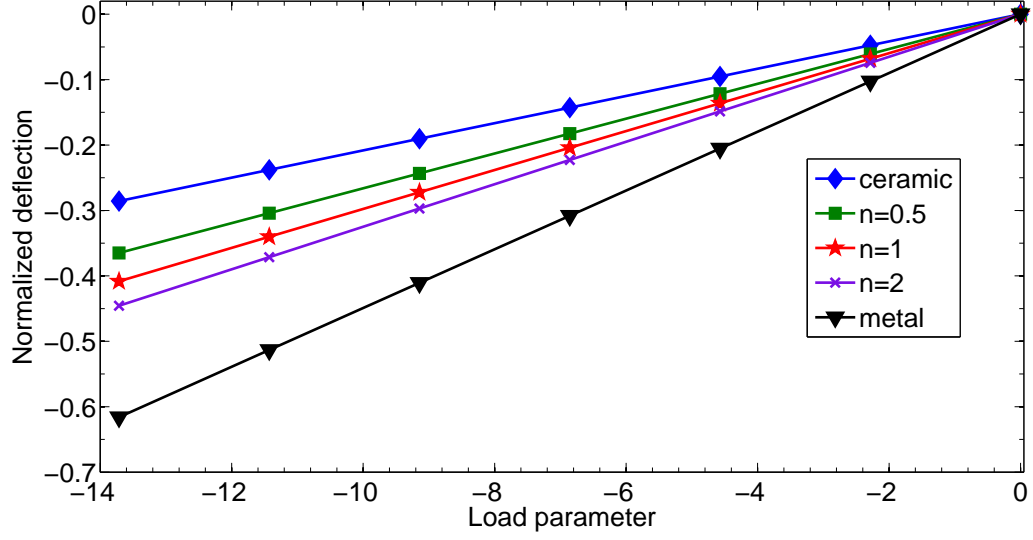
24

Figure 5: The normalized axial stress $\overline{\sigma}_{xx} = \sigma_{xx}\frac{h^2}{pL^2}$ at points on the vertical line passing through the centroid of a simply supported square Al/Zr0$_2$ FGM plate subjected to uniform mechanical load p.

$n = 1$ is minimum. Generally, it can be seen that the deflections of the FGM plates are much lower than those of isotropic plates (*i.e.*, $n = 0$), which implies high temperature resistance behaviour of the functionally graded plates.

Now, we investigate the FGM plate under thermo-mechanical loads. The temperature at the top surface of the plate is held at 300°C (top surface is assumed to be rich in ceramic) and the temperature at the bottom surface (assumed to be rich in metal) is $T_m =$20°C. Figure (9) shows the center deflection $\overline{w}_c = w_c/h$ of the plate with respect to various load parameters $\overline{p} = pa^4/(E_m h^4)$ given in the interval -14 $\leq \overline{p} \leq$ 0 for different values of the gradient index. It can be seen that the central deflection of the plate is completely different from the case with a purely mechanical loading (see Figure (6)). However, similarly to the case of the FGM plate under pure mechanical loading, the center deflection of the plate linearly increases with the load. The metallic phase shows the maximum range of deflection changes and the ceramic plate the least.

Figure (9) plots the distribution of axial stress through the thickness of the plate under the uniform mechanical

25

(a)
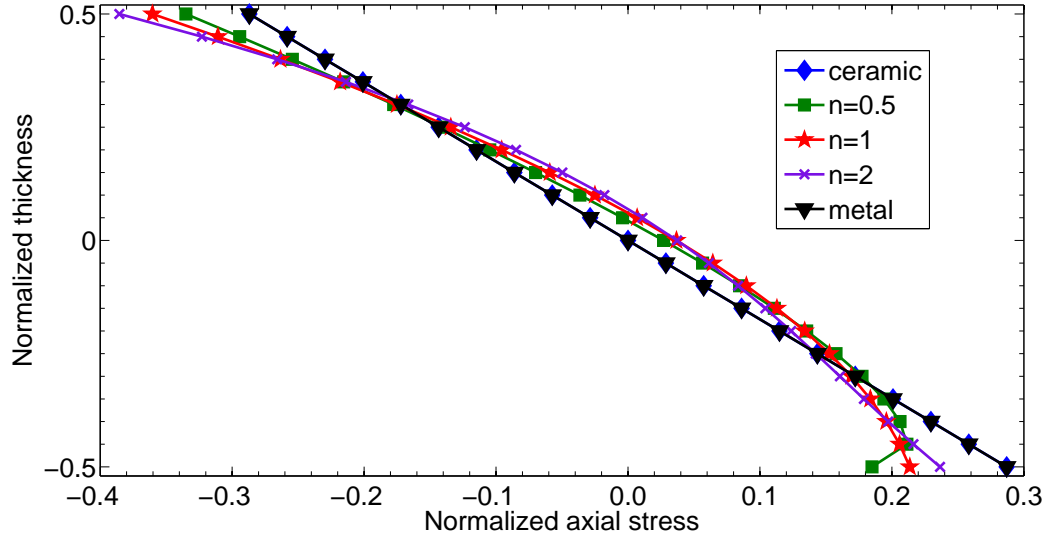
(b)

Figure 6: The normalized center deflection $\overline{w}_c$ and the normalized axial stress $\overline{\sigma}_{xx}$ of a simply supported square Al/Zr0$_2$ FGM plate subjected to uniform mechanical load p: (a)The normalized center deflection, $\overline{w}_c = w_c/h$ with $\overline{p} = pa^4/(E_m h^4)$ and (b) The normalized axial stress $\overline{\sigma}_{xx} = \sigma_{xx}\frac{h^2}{pa^2}$ at points on the vertical line passing through the centroid with load p.
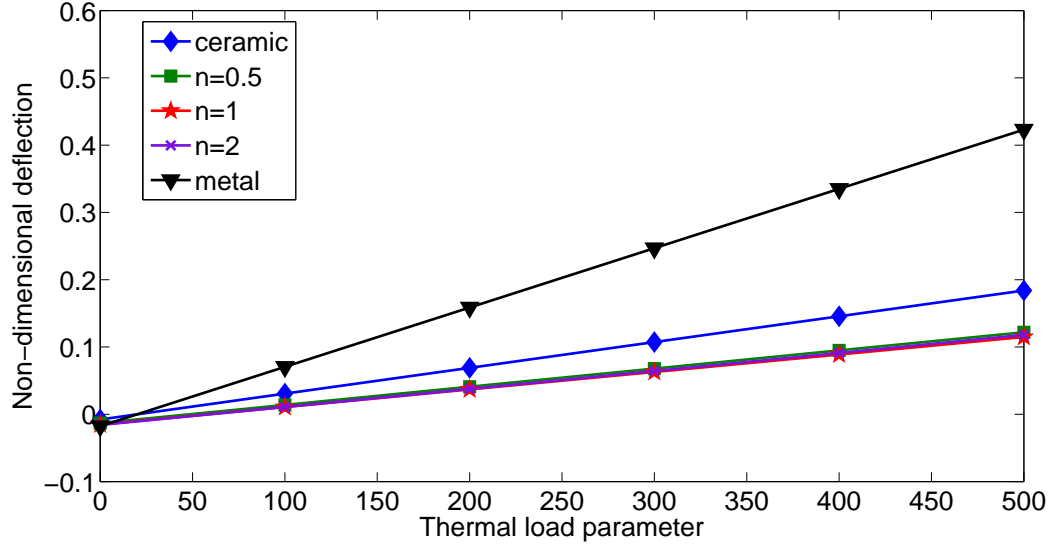
Figure 7: The normalized center deflection $\overline{w}_c = w_c/h$ of a simply supported square Al/ZrO$_2$ FGM plate subjected to thermal load.
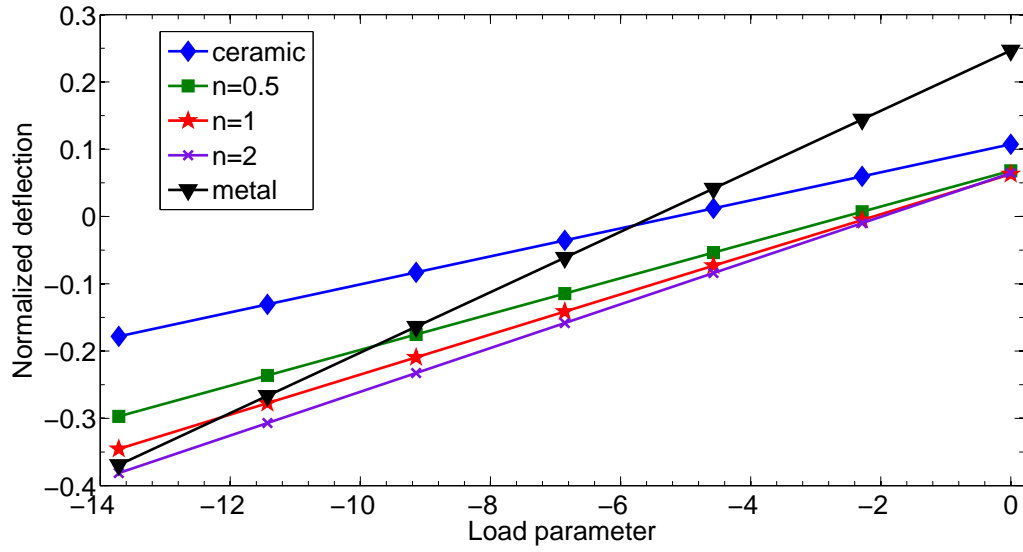
Figure 8: The normalized center deflection $\overline{w}_c = w_c/h$ of a simply supported square Al/ZrO$_2$ FGM plate subjected to thermo-mechanical load.
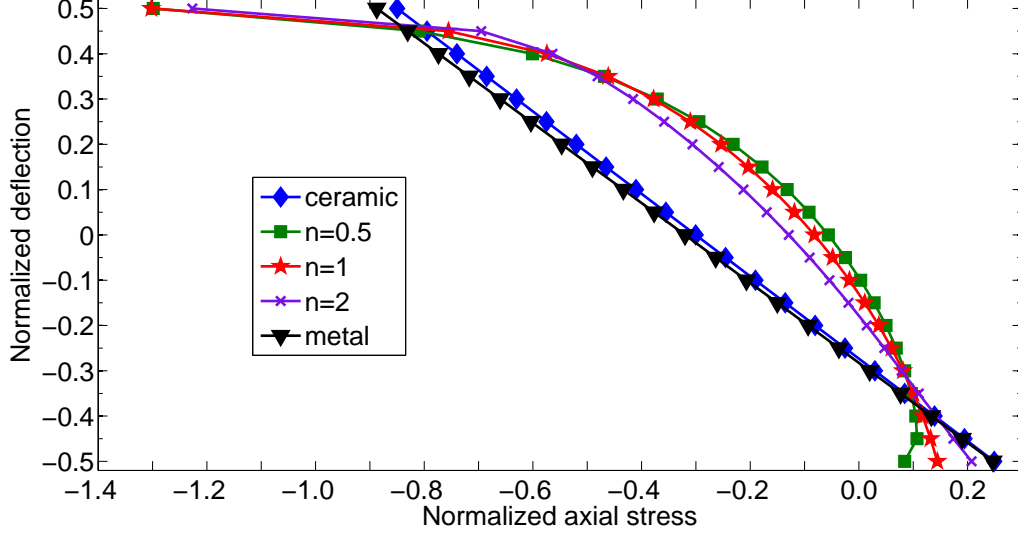
Figure 9: The normalized center deflection $\overline{w}_c = w_c/h$ of a simply supported square Al/ZrO$_2$ FGM plate subjected to thermo-mechanical load.

load $p = $ -10^6 N/m^2. Comparing to Figure (6) for purely mechanical load, it is seen that the maximum compressive stress at the top surface of the plate has been obtained for the FGM plate with a gradient index $n = 1$. Again, the metallic or ceramic plate shows the minimum tensile stress at the bottom surface. Note that the results match very well with those given in [51, 48].

Skew plates

In this example, we study the behaviour of FGM skew plates under mechanical loads. A simply supported Al/ZrO$_2$ FGM skew plate with length $a = $ 10m and thickness $h = $ 0.1m is considered. The plate is subjected to a uniform mechanical load $p = $ -10^4 N/m^2. A mesh of quadratic NURBS elements with 17 × 17 control points is used for modelling the plate. Figure (10) shows the distribution of non-dimensional axial stress $\overline{\sigma}_{xx} = \sigma_{xx}h^2/(pa^2)$ through the thickness of the plate for different skew angles with gradient index $n = 0.5$. It can be observed that the axial stresses increase as the skew angle decreases. Similar behaviour can be found for gradient indices $n = 1$ and $n = 2$ in Figures 11 and 12, respectively. The results obtained by our isogeometric

28

analysis are in a good agreement with those reported in [47] using the element free $kp-$ Ritz method and the results of NS-DSG3 [48] and ES-DSG3 [52].
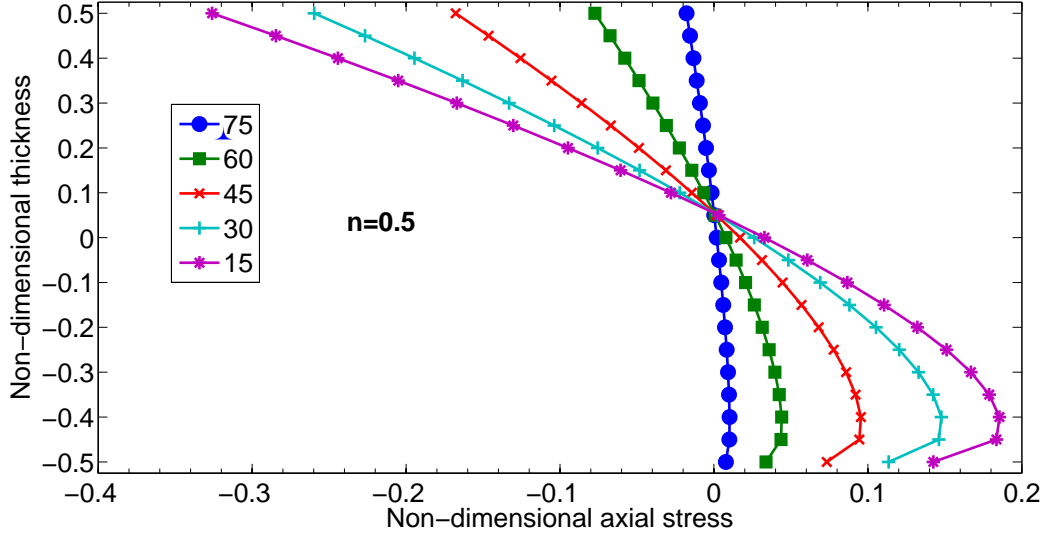

Figure 10: The effect of skew angle on the axial stress $\overline{\sigma}_{xx} = \sigma_{xx}\frac{h^2}{pL^2}$ profile for simply supported FGM Al/ZrO$_2$ subjected to a mechanical load with gradient index $n = 0.5$.

5.2. Free flexural vibrations

In this section, the free flexural vibration characteristics of FGM plates are studied numerically. In all cases, we present the non-dimensionalized free flexural frequency defined as, unless otherwise stated:

$$\overline{\omega} = \omega h \sqrt{\frac{\rho_c}{E_c}} \tag{42}$$

where ω is the natural frequency, ρ_c, E_c are the mass density and Young's modulus of the ceramic phase. Before proceeding with a detailed study on the effect of gradient index on the natural frequencies, the formulation developed herein is validated against available analytical/numerical solutions in the literature.
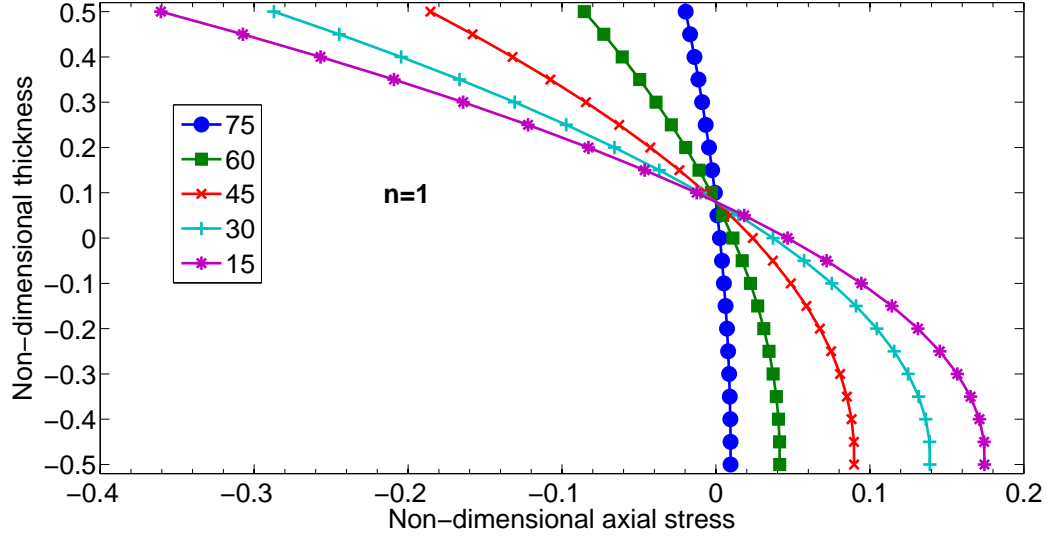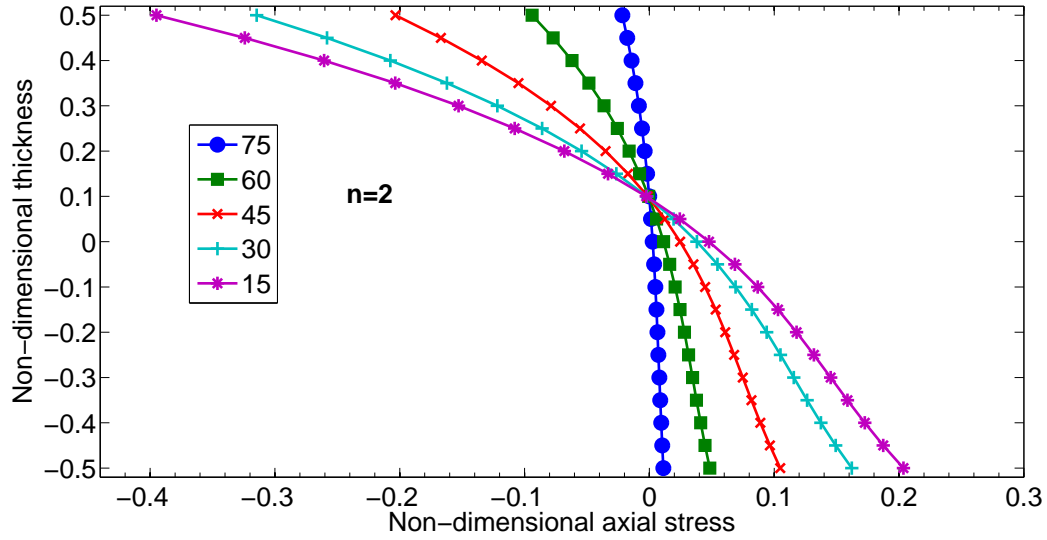
29

Figure 11: The effect of skew angle on the axial stress $\overline{\sigma}_{xx} = \sigma_{xx}\frac{h^2}{pL^2}$ profile for simply supported FGM Al/ZrO$_2$ subjected to a mechanical load with gradient index $n = 1.0$.

Figure 12: The effect of skew angle on the axial stress $\overline{\sigma}_{xx} = \sigma_{xx}\frac{h^2}{pL^2}$ profile for simply supported FGM Al/ZrO$_2$ subjected to a mechanical load with gradient index $n = 2.0$.

Square plates

A simply supported Al/Al_2O_3 FGM square plate with various length-to-thickness ratio is considered. The plate is modelled employing quadratic, cubic and quartic NURBS elements with meshes of 8, 14 and 20 control points per side. The results obtained from the isogeometric analysis for the first normalized frequency parameter $\overline{\omega}$ are presented in Tables 5 and 6 for different plate aspect ratios ($a/h = 5, 10, 20$) and compared with the results available in the literature [21, 52, 53, 54]. The first normalized frequency ($= \overline{\omega}/\omega_{analytical}$) is shown in Figures 13 - Figure (15) for various a/h ratios ($a/h = 5, 10, 20$). The results of IGA shown in these figures are computed using quadratic NURBS elements with 14 control points per side. It is seen that the results from IGA are superior ~~to~~ compared to other methods, irrespective of the material gradient index.
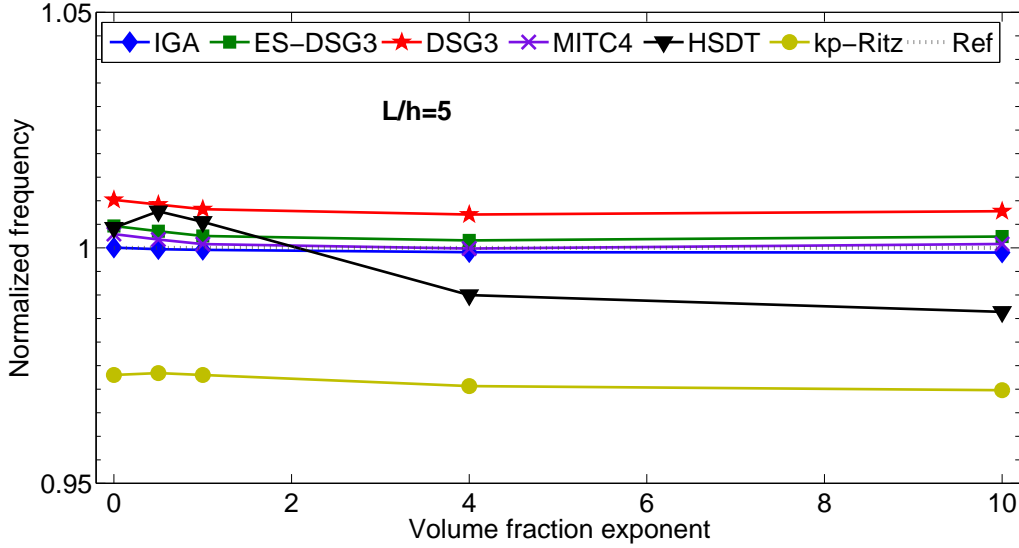

Figure 13: The normalized first frequency $\omega^* = \omega/\omega_{ref}$ versus volume fraction exponents for SSSS Al/Al_2O_3 FGM plate with $a/h = 5$. The frequency is normalized with the analytical solution.

Figures 16 - (17) shows the first four non-dimensionalized frequencies for a Al/ZrO_2 FGM plate with $a/h = 10$ with various boundary conditions (CCCC, SSSS and ~~CFFF~~). It can be seen that very good agreement is obtained with the results available in the literature. For CFFF boundary conditions, the difference between the
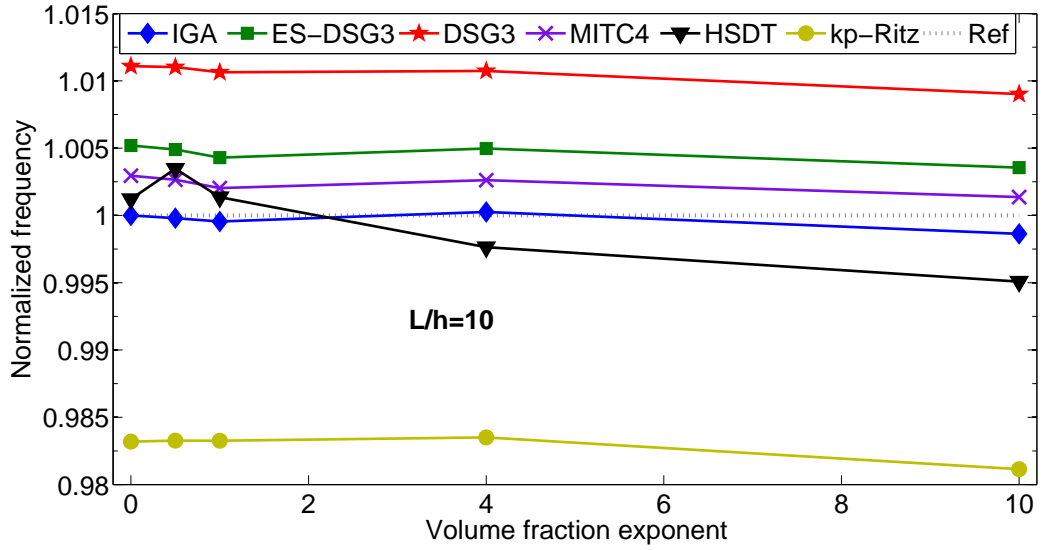
Figure 14: The normalized first frequency $\omega^* = \omega/\omega_{\mathrm{ref}}$ versus volume fraction exponents for SSSS Al/Al$_2$O$_3$ FGM plate with $a/h = 10$. The frequency is normalized with the analytical solution.
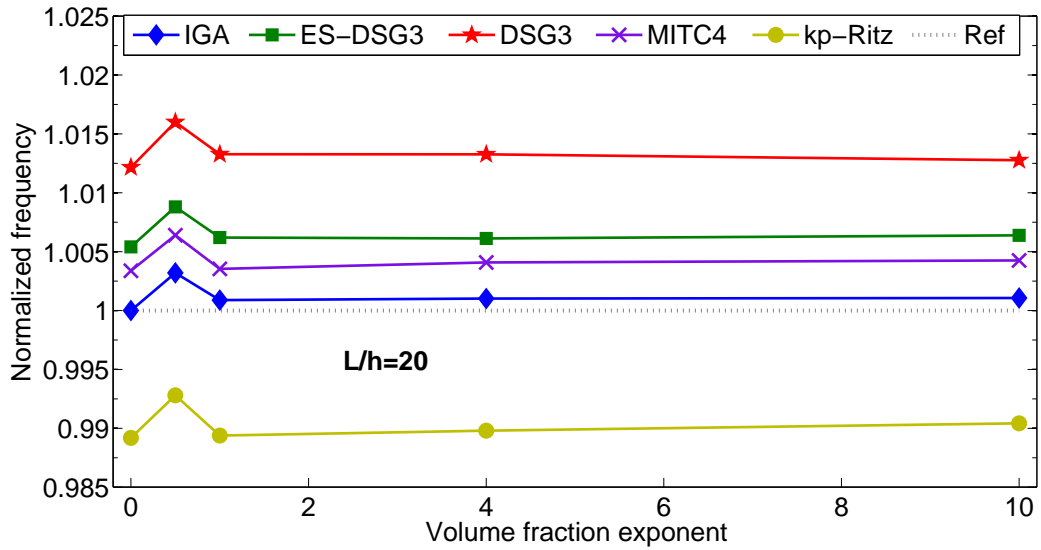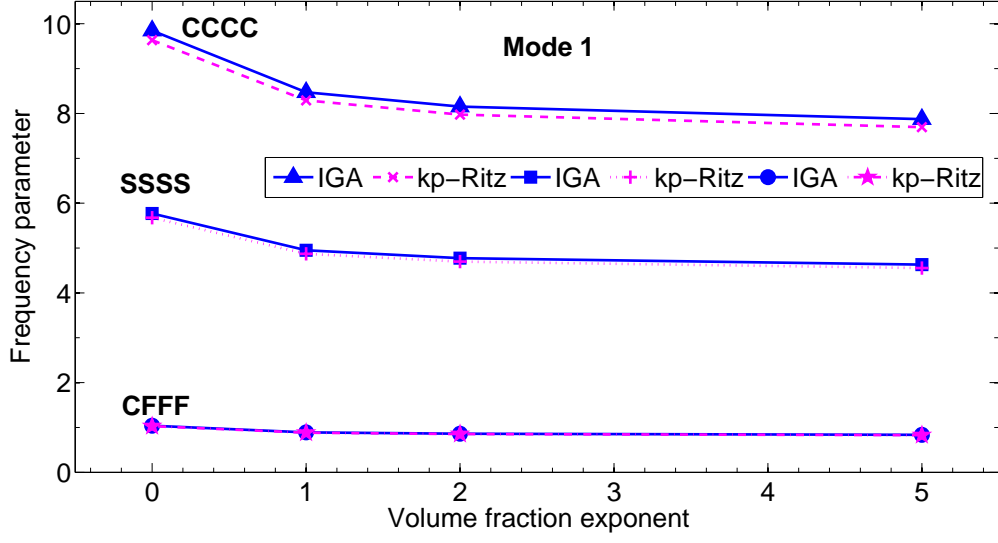

Figure 15: The normalized first frequency $\omega^* = \omega/\omega_{\mathrm{ref}}$ versus volume fraction exponents for SSSS Al/Al$_2$O$_3$ FGM plate with $a/h = 20$. The frequency is normalized with the analytical solution.
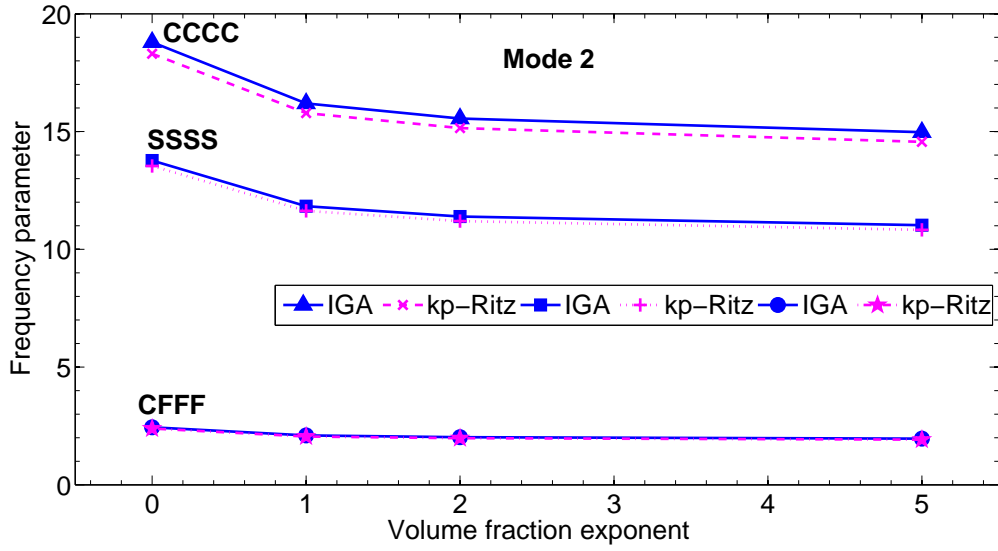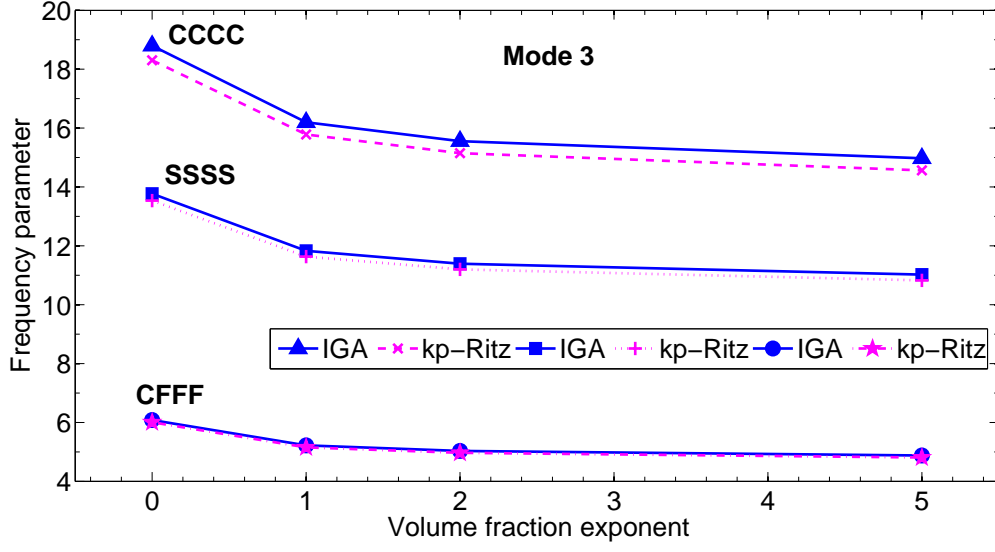
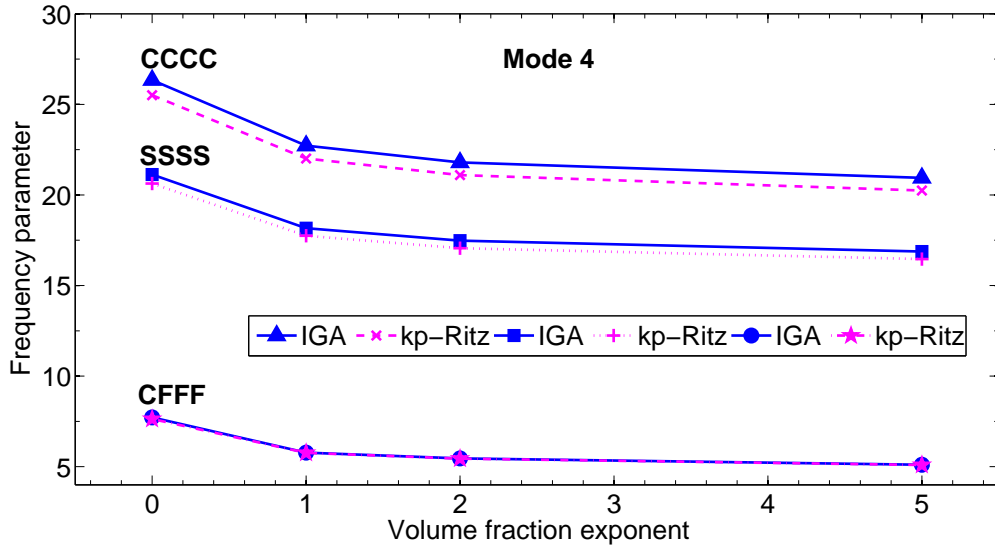Figure 16: The non-dimensional frequency $\overline{\omega} = \frac{\omega a^2}{h}\sqrt{\frac{\rho_c}{E_o}}$ versus various volume fraction exponent of Al/ZrO$_2$ FGM plate with different boundary conditions: (a) Mode 1 and (b) Mode 2.

Figure 17: The non-dimensional frequency $\overline{\omega} = \frac{\omega a^2}{h}\sqrt{\frac{\rho_c}{E_o}}$ versus various volume fraction exponent of Al/ZrO$_2$ FGM plate with different boundary conditions: (a) Mode 3 and (b) Mode 4.

IGA and the element free $kp-$Ritz is ranged from 0.3% to 2.1%, while it is about 2.2 - 3.3% and 1.6 - 2.5% for CCCC and SSSS boundary conditions, respectively. Note that all the present results agree very well with those given in [48, 52].

Table 5: The first normalized frequency parameter $\overline{\omega} = \omega h \sqrt{\frac{\rho_c}{E_c}}$ for fully simply supported Al/Al$_2$O$_3$ FGM square plate for $a/h = 5$.

Method	Control points	gradient index n				
		0	0.5	1	4	10
	8	0.21128	0.18051	0.16309	0.13962	0.13231
IGA-Quadratic	14	0.21121	0.18045	0.16303	0.13957	0.13227
	20	0.21121	0.18044	0.16303	0.13957	0.13227
	8	0.21121	0.18044	0.16303	0.13957	0.13227
IGA-Cubic	14	0.21121	0.18044	0.16303	0.13957	0.13227
	20	0.21121	0.18044	0.16303	0.13957	0.13227
	8	0.21121	0.18044	0.16303	0.13957	0.13227
IGA-Quartic	14	0.21121	0.18044	0.16303	0.13957	0.13227
	20	0.21121	0.18044	0.16303	0.13957	0.13227
ES-DSG3 (20×20) [52]		0.21218	0.18114	0.16351	0.13992	0.13272
DSG3 (16×16) [52]		0.21335	0.18216	0.16444	0.14069	0.13343
MITC4 (16×16) [52]		0.21182	0.18082	0.16323	0.13968	0.13251
HSDT [21]		0.21210	0.18190	0.16400	0.13830	0.13060
$kp-$Ritz [53]		0.20550	0.17570	0.15870	0.13560	0.12840
Ref. [54]		0.21120	0.18050	0.16310	0.13970	0.13240

Skew plate

Next, the effects of the skewness of the plate on the free flexural vibration of the FGM plate is studied. A Al/ZrO$_2$-2 skew FGM plate with length-to-thickness ratio $a/h = 10$ and various skew angles are considered

Table 6: The first normalized frequency parameter $\overline{\omega} = \omega h \sqrt{\frac{\rho_c}{E_c}}$ for fully simply supported Al/Al$_2$O$_3$ FGM square plate for $a/h =$ 10, 20.

a/h	Method	gradient index n				
		0	0.5	1	4	10
10	IGA-Quadratic (20 points)	0.05769	0.04899	0.4418	0.03821	0.03655
	IGA-Cubic (20 points)	0.05769	0.04898	0.04417	0.03821	0.03655
	IGA-Quartic (20 points)	0.05769	0.04898	0.04417	0.03821	0.03655
	ES-DSG3 (20×20) [52]	0.05800	0.04924	0.04439	0.03839	0.03973
	DSG3 (16×16) [52]	0.05834	0.04954	0.04467	0.03861	0.03693
	MITC4 (16×16) [52]	0.05787	0.049132	0.04429	0.03830	0.03665
	HSDT [21]	0.05777	0.04917	0.04426	0.03811	0.03642
	$kp-$Ritz [53]	0.05673	0.04818	0.04346	0.3757	0.03591
	Ref. [54]	0.05770	0.04900	0.04420	0.03820	0.03660
20	IGA-Quadratic (20 points)	0.01480	0.01254	0.01130	0.00981	0.00944
	IGA-Cubic (20 points)	0.01480	0.01254	0.01130	0.00981	0.00944
	IGA-Quartic (20 points)	0.01480	0.01254	0.01130	0.00981	0.00944
	ES-DSG3 (20×20) [52]	0.01488	0.01261	0.01137	0.00986	0.00946
	DSG3 (16×16) [52]	0.01498	0.012704	0.01145	0.00993	0.00952
	MITC4 (16×16) [52]	0.01485	0.01258	0.01134	0.00984	0.00944
	$kp-$Ritz [53]	0.01464	0.01241	0.01118	0.00970	0.00931
	Ref. [54]	0.01480	0.01250	0.01130	0.00980	0.00940

in this example. The skew plate is modelled using quadratic NURBS elements with 17×17 control points. The first two non-dimensionalized frequencies are shown in Figures 18 - (19) for SSSS and CCCC boundary conditions, respectively. For comparison, the results from the element free $kp-$Ritz [53] are also plotted. From the figures, it is seen that the IGA gives higher frequencies than the element free $kp-$Ritz method. It is also observed that by increasing the gradient index or decreasing the skew angle, the frequency decreases. In both cases, the decrease in the natural frequency can be attributed to the stiffness degradation. In the case of gradient index, the stiffness degradation is due to increased metallic volume fraction, while the geometry of the plate is a contributing factor in decreasing the frequency when the skew angle decreases. The first eight mode shapes of fully clamped Al/ZrO$_2$-2 skew plate with skew angle $\psi = 45°$ and gradient index $n = 0.5$ is plotted in Figure (20).

Remark 5.1. In the next two sections, the present formulation is extended to study the buckling and flutter characteristics of the the FGM plates. For the whole, quadratic NUBRS functions with 17×17 control points are used, unless otherwise specified.

5.3. Buckling analysis

In this section, we present the mechanical and thermal buckling behaviour of functionally graded skew plates. The FGM plate considered here consists of aluminum and alumina (see Table 1 for material properties).

Mechanical Buckling

The critical buckling parameters are defined for uni- and bi- axial compressive loads as:

$$\lambda_{\text{cru}} = \frac{N^0_{\text{xxcr}} b^2}{\pi^2 D_c}$$
$$\lambda_{\text{crb}} = \frac{N^0_{\text{yycr}} b^2}{\pi^2 D_c} \tag{43}$$
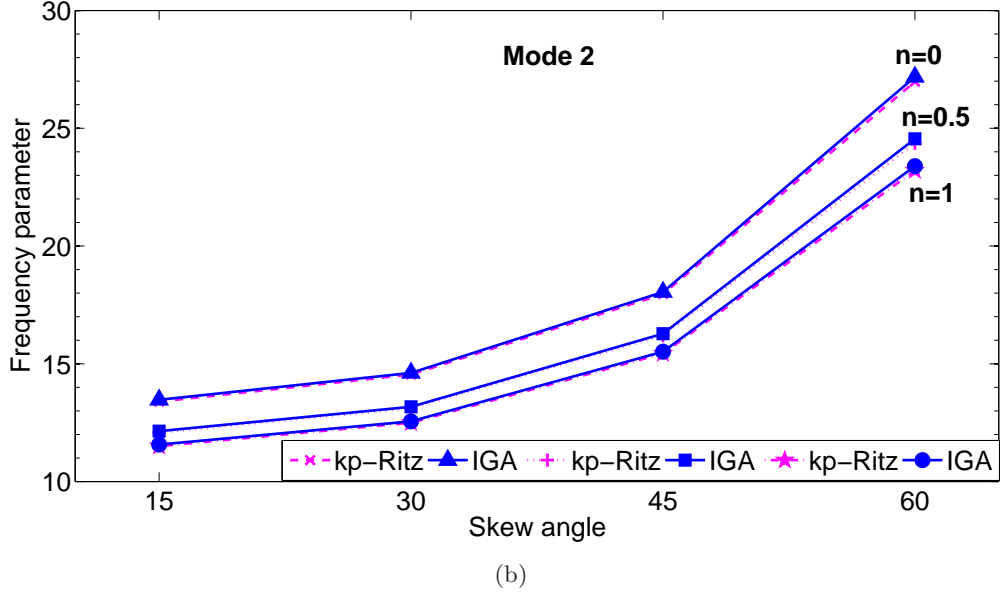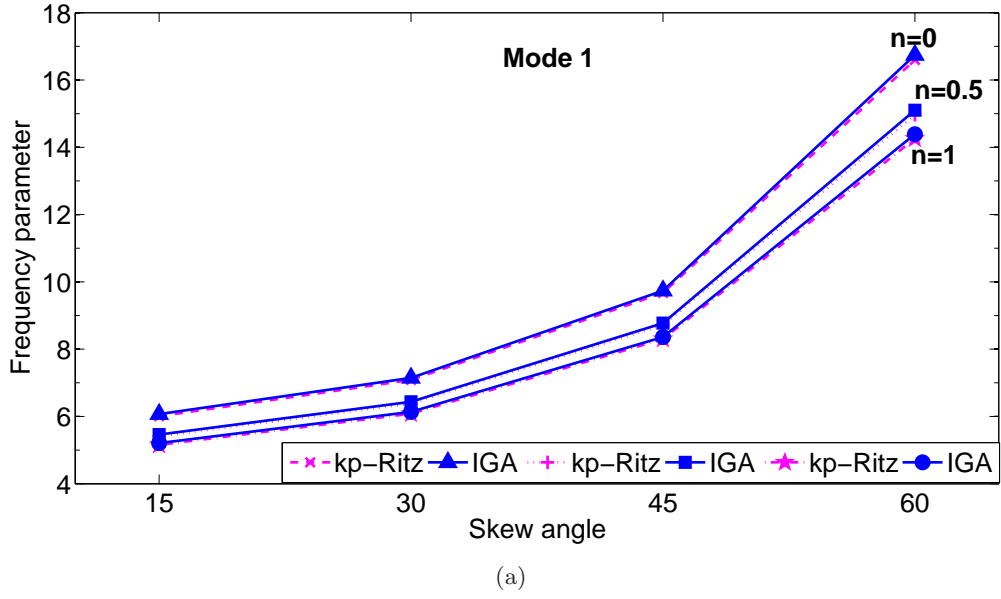
(a)

(b)

Figure 18: The non-dimensional frequency $\overline{\omega} = \omega a^2 \sqrt{\rho_c/E_c}$ for a simply supported Al/ZrO$_2$-2 skew plate versus various skew angles for different values of gradient index with $a/h = 10$.
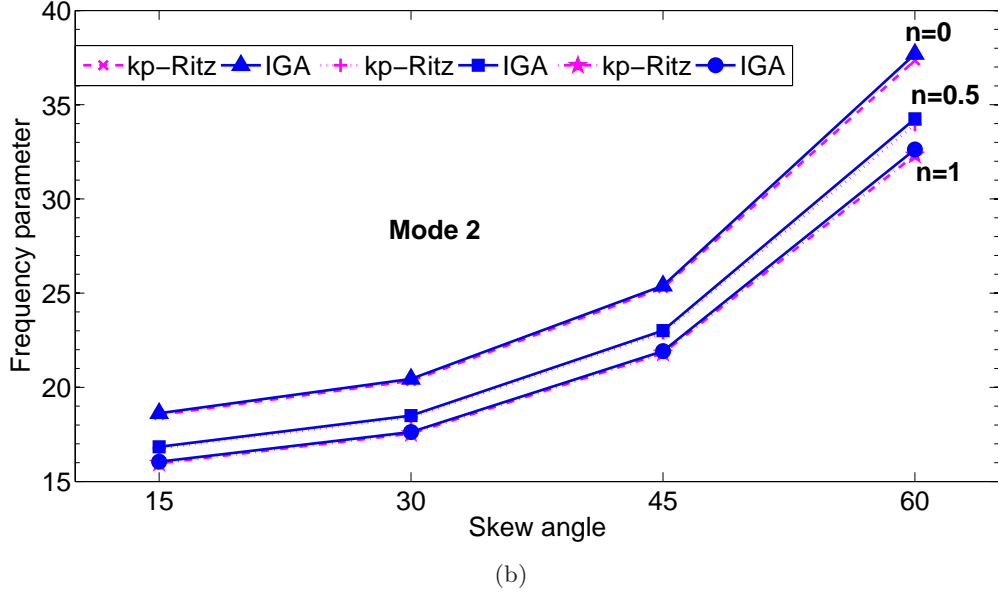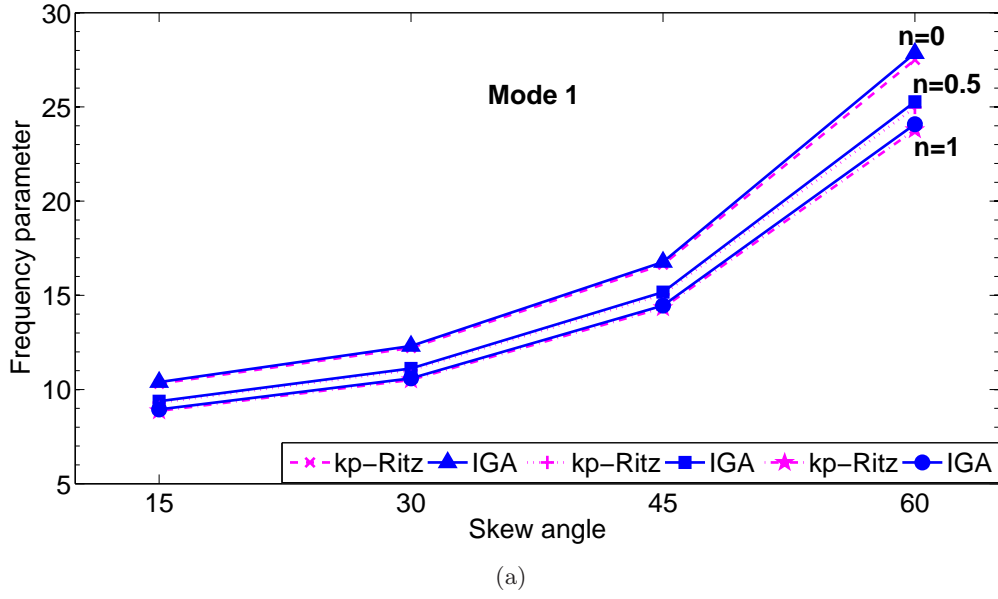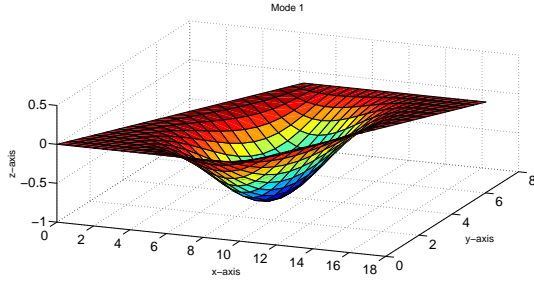
(a)

(b)

Figure 19: The non-dimensional frequency $\overline{\omega} = \omega a^2 \sqrt{\rho_c/E_c}$ for a clamped Al/ZrO$_2$-2 skew plate versus various skew angles for different values of gradient index with $a/h = 10$.

39

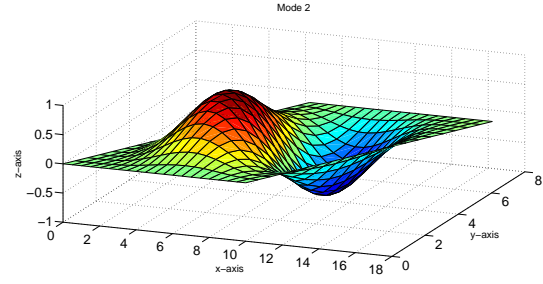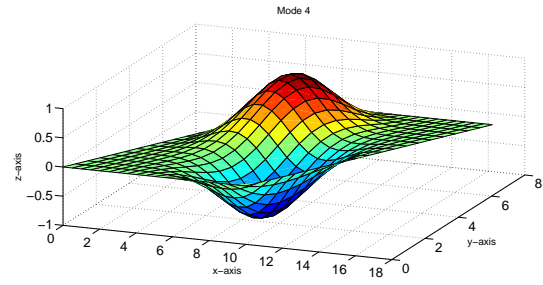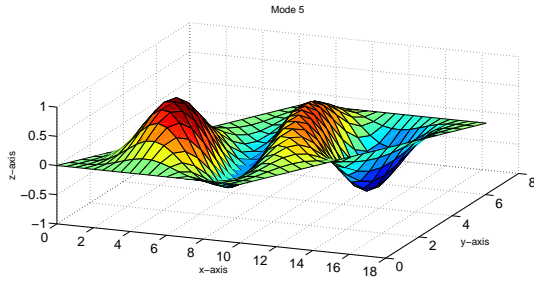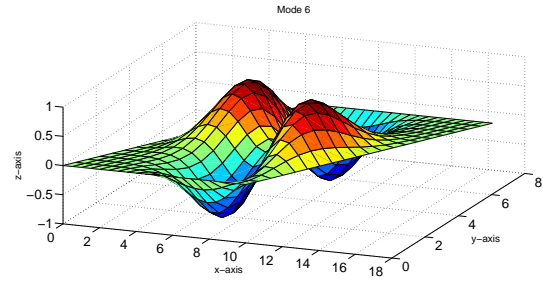(a) mode 1
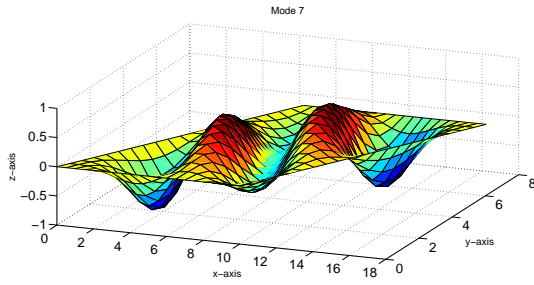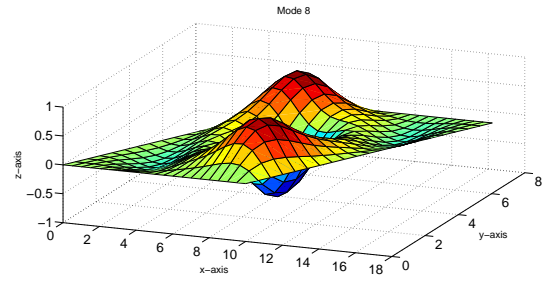
(b) mode 2
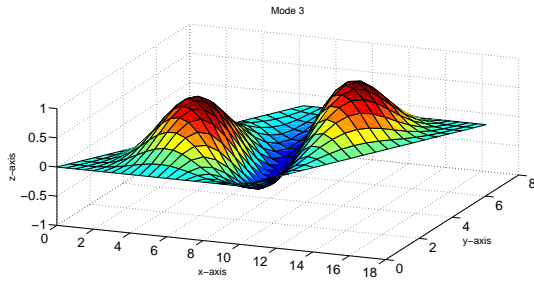
(c) mode 3

(d) mode 4

(e) mode 5

(f) mode 6

(g) mode 7

(h) mode 8

Figure 20: First eight mode shapes for a clamped Al/Zro$_2$ skew plate with $a/h = 10$, gradient index $n = 0.5$ and $\psi = 45°$.

where, $D_c = E_c h^3/(12(1 - \nu^2))$. The critical buckling loads evaluated by varying the skew angle of the plate, volume fraction index and considering mechanical loads such as uni- and biaxial compressive loads are shown in Tables 7 - 8 for two different thickness ratios. The efficacy of the present formulation is demonstrated by comparing our results with those in [8]. It can be seen that increasing the gradient index decreases the critical buckling load. It is also observed that the decrease in the critical value is significant for the material gradient index $n \leq 2$ and that further increase in n yields less reduction in the critical value, irrespective of the skew angle.

Table 7: Critical buckling parameters for a thin simply supported FGM skew plate with $a/h = 100$ and $a/b = 1$.

Skew angle	λ_{cr}	Gradient index, n						
		0		1		2	5	10
		Ref. [8]	Present	Ref. [8]	Present			
0°	λ_{cru}	4.0010	3.9998	1.7956	1.8034	1.5320	1.2606	1.0830
	λ_{crb}	2.0002	1.9999	0.8980	0.9017	0.7660	0.6303	0.5415
15°	λ_{cru}	4.3946	4.3946	1.9716	1.9716	1.6752	1.3800	1.1868
	λ_{crb}	2.1154	2.1154	0.9517	0.9517	0.8086	0.6652	0.5716
30°	λ_{cru}	5.8966	5.8966	2.6496	2.6496	2.2515	1.8607	1.6032
	λ_{crb}	2.5365	2.5365	1.1519	1.1519	0.9788	0.8044	0.6905
45°	λ_{cru}	10.1031	10.1031	4.5445	4.5445	3.8625	3.2234	2.7964
	λ_{crb}	3.6399	3.6399	1.6863	1.6863	1.4330	1.1774	1.0103

Thermal Buckling

The temperature rise of $T_m = 5°\mathrm{C}$ in the metal-rich surface of the plate is assumed in the present study. In addition to nonlinear temperature distribution across the plate thickness, the linear case is also considered in the present analysis by truncating the higher order terms in Equation (9). The plate is of uniform thickness and simply supported on all four edges. The critical buckling temperature difference ΔT_{cr} using two values of the

Table 8: Critical buckling parameters for a thick simply supported FGM skew plate with $a/h = 10$ and $a/b = 1$.

Skew angle	λ_{cr}	Gradient index, n						
		0		1		2	5	10
		Ref. [8]	Present	Ref. [8]	Present			
$0°$	λ_{cru}	3.7374	3.7307	1.6892	1.6793	1.4198	1.1632	0.9999
	λ_{crb}	1.8686	1.8654	0.8449	0.8397	0.7099	0.5816	0.4999
$15°$	λ_{cru}	4.0791	4.0791	1.8458	1.8458	1.5616	1.2810	1.1021
	λ_{crb}	1.9660	1.9660	0.8923	0.8923	0.7550	0.6184	0.5315
$30°$	λ_{cru}	5.3571	5.3571	2.4298	2.4298	2.0533	1.6886	1.4565
	λ_{crb}	2.3226	2.3226	1.0659	1.0659	0.9011	0.7367	0.6326
$45°$	λ_{cru}	8.5261	8.5261	3.8835	3.8835	3.2679	2.7046	2.3521
	λ_{crb}	3.1962	3.1962	1.5030	1.5030	1.2680	1.0335	0.8871

aspect ratio $a/b = 1$ and 2 with $a/h = 10$ and for various skew angles is given in Table 9. It can been seen that the results from the present formulation are in good agreement with the results available in the literature. The decrease in the critical buckling load with the material gradient index n is attributed to the stiffness degradation due to the increase in the metallic volume fraction. The thermal stability of the plate increases with the skew angle of the plate and the same behavior is observed for other values of gradient index n. It can also be seen that the nonlinear temperature variation through the thickness yields higher critical values compared to the linear distribution case.

5.4. Flutter analyses

In this section, the present formulation is extended to analyse the flutter characteristics of functionally graded material plates. Both simply supported and clamped boundary conditions are considered in this study and the flow direction is assumed to be at right angles to the plate. Only square plate is considered and the results are presented only for $a/h = 100$. It should be noted that the present formulation is not limited to this alone. In

Table 9: Critical buckling temperature ΔT_{cr} for a thin simply supported FGM skew plate with $a/h = 100$ and $a/b = 1$ under linear and nonlinear temperature rise through the thickness of the plate.

a/b	Skew angle	Temperature rise	Gradient index, n				
			0				
			Ref. [55]	Present	0.5	1	5
1	0°	Linear	24.1951	24.1912	9.3787	5.5207	3.8987
		Nonlinear	24.1951	24.1912	12.3629	7.6615	4.8740
	30°	Linear	33.9558	33.9503	14.9115	9.7737	7.4681
		Nonlinear	33.9558	33.9503	19.6600	13.558	9.3399
	60°	Linear	123.0974	123.1172	65.4519	48.6271	40.0647
		Nonlinear	123.0974	123.1172	86.2949	67.4989	50.1064
2	0°	Nonlinear	75.4278	75.4475	50.6564	38.6525	28.3067
	30°	Nonlinear	100.9349	100.9512	69.7225	54.0838	39.9718
	60°	Nonlinear	304.6912	304.6421	222.0921	177.4280	133.1456

all cases, we present the non dimensionalized critical aerodynamic pressure, λ_{cr} and critical frequency ω_{cr} as, unless specified otherwise:

$$\Omega_{cr} = \omega_{cr} a^2 \sqrt{\frac{\rho_c h}{D_c}}$$

$$\lambda_{cr} = \lambda_{cr} \frac{a^3}{D_c} \tag{44}$$

where $D_c = \frac{E_c h^3}{12(1-\nu_c^2)}$ is the bending rigidity of the plate, E_c, ν_c are the Young's modulus and Poisson's ratio of the ceramic material and ρ_c is the mass density. In order to be consistent with the existing literature, properties of the ceramic are used for normalization.

Table 10: Comparison of critical aerodynamic pressure and coalescence frequency for an isotropic plate with various boundary conditions ($a/b = 1, a/h = 100, \nu = 0.3, \theta' = 0$).

Reference	Flutter bounds	Boundary condition	
1	1	Simply supported	Clamped
Ref. [27]	λ_{cr}	511.11	852.34
	ω_{cr}	1840.29	4274.32
Present	λ_{cr}	511.92	854.88
	ω_{cr}	1844.80	4305.30

Before proceeding with the detailed study, the formulation developed herein is validated against available results pertaining to the critical aerodynamic pressure and critical frequency for an isotropic plate with and without a crack. The computed critical aerodynamic pressure and the critical frequency for an isotropic square plate with various boundary conditions is given in Table 10. Next, the influence of boundary conditions on the flutter characteristics is studied. For this study, consider a square FGM plate made up of Aluminum-Alumina with $a/h = 100$. Figure (21) shows the influence of the boundary conditions on the critical aerodynamic pressure for various gradient index. It can be seen that the critical pressure is more for the clamped plate in comparison

with that of the simply supported plate as expected. It is also seen that the aerodynamic pressure decreases with increase in the gradient index n. However the rate of decrease is high for low values of n. This can be attributed to the fact that the stiffness is ~~high~~ for the ceramic plate and minimum for the metallic plate and it degrades gradually with increase in the gradient index n.
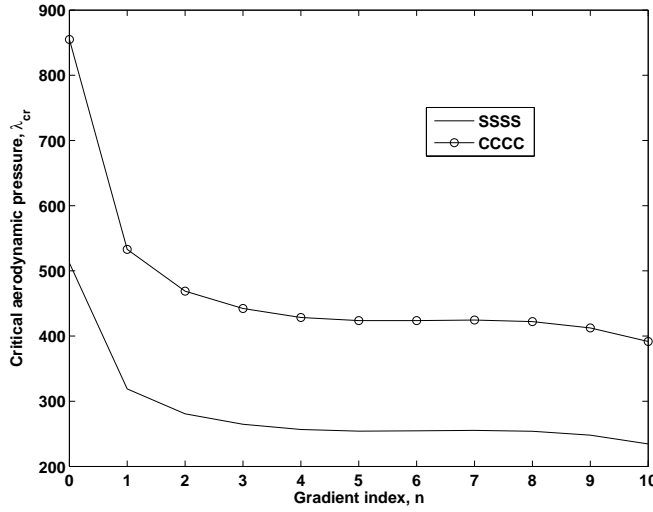

Figure 21: Effect of boundary conditions on the critical aerodynamic pressure λ_{cr}

6. Conclusions

In this paper, we applied the NURBS based Bubnov-Galerkin iso-geometric finite element method to study the static and dynamic response of functionally graded material plates. The first order shear deformation plate theory (FSDT) was used to describe the plate kinematics. Of course the present method is not limited to FSDT and can easily be extended to higher order plate theories. It is to be noted that with NURBS basis functions, geometry could be exactly represented. Although in the present study only simple geometries are considered, the only thing that would change is the information pertaining to the geometry represented by the NURBS basis functions, when it is applied to model and/or analyze complex geometries. The formulation when applied

45

to thin plates, suffers from shear locking, which is alleviated by employing a modified shear correction factor. Numerical experiments have been conducted to bring out the influence of the gradient index, the plate aspect ratio and the plate thickness on the global response of functionally graded material plates. From the detailed numerical study, it can be concluded that with increasing gradient index n, the static deflection increases, while the free flexural vibration, critical buckling load and the flutter frequency decreases. This can be attributed to the reduction in stiffness of the material structure due to increase in the metallic volume fraction.

Acknowledgements

Reference

[1] M. Koizumi, The concept of FGM, Ceramic Transactions - Functionally graded materials 34 (1993) 3–10.

[2] J. N. Reddy, Analysis of functionally graded plates, International Journal for Numerical Methods in Engineering 47 (2000) 663–684.

[3] J. Yang, H. S. Shen, Vibration characteristic and transient response of shear-deformable functionally graded plates in thermal environments, Journal of Sound and Vibration 255 (2002) 579–602.

[4] N. Sundararajan, T. Prakash, M. Ganapathi, Nonlinear free flexural vibrations of functionally graded rectangular and skew plates under thermal environments, Finite Elements in Analysis and Design 42 (2) (2005) 152–168.

[5] L. C. Qian, R. C. Batra, L. M. Chen, Static and dynamic deformations of thick functionally graded elastic plates by using higher order shear and normal deformable plate theory and meshless local Petrov Galerkin method, Composites Part B: Engineering 35 (2004) 685–697.

[6] A. J. M. Ferreira, R. C. Batra, C. M. C. Roque, L. K. Qian, R. M. N. Jorge, Natural frequencies of functionally graded plates by a meshless method, Composite Structures 75 (2006) 593–600.

[7] S. Natarajan, G. Manickam, Bending and vibration of functionally graded material sandwich plates using an accurate theory, Finite Elements in Analysis and Design 57 (2012) 32–42.

[8] M. Ganapathi, T. Prakash, N. Sundararajan, Influence of functionally graded material on buckling of skew plates under mechanical loads, ASCE Journal of Engineering Mechanics 132 (2006) 902–905.

[9] K. J. Bathe, E. Dvorkin, A four node plate bending element based on Mindlin - Reissner plate theory and mixed interpolation., International Journal for Numerical Methods in Engineering 21 (1985) 367–383.

[10] B. R. Somashekar, G. Prathap, C. R. Babu, A field-consistent four-noded laminated anisotropic plate/shell element, Computers and Structures 25 (1987) 345–353.

[11] M. Ganapathi, T. K. Varadan, B. S. Sarma, Nonlinear flexural vibrations of laminated orthotropic plates, Computers and Structures 39 (1991) 685–688.

[12] K. U. Bletzinger, M. Bischoff, E. Ramm, A unified approach for shear-locking free triangular and rectangular shell finite elements, International Journal for Numerical Methods in Engineering 75 (2000) 321–334.

[13] D. Wang, J. S. Chen, Locking-free stabilized conforming nodal integration for mesh-free Mindlin-Reissner plate formulation, Computer Methods in Applied Mechanical and Engineering 193 (2004) 1065–1083.

[14] N. T. Nguyen, T. Rabczuk, H. Nguyen-Xuan, S. Bordas, A smoothed finite element method for shell analysis, Computer Methods in Applied Mechanics and Engineering 198 (2008) 165–177.

[15] H. Nguyen-Xuan, T. Rabczuk, S. Bordas, J. F. Debongnie, A smoothed finite element method for plate analysis, Computer Methods in Applied Mechanics and Engineering 197 (2008) 1184–1203.

[16] W. Kanok-Nukulchai, W. Barry, K. Saran-Yasoontorn, P. H. Bouillard, On elimination of shear locking in the element-free Galerkin method, International Journal for Numerical Methods in Engineering 52 (2001) 705–725.

[17] X. Q. He, T. Y. Ng, S. Sivashanker, K. M. Liew, Active control of FGM plates with integrated piezoelectric sensors and actuators, International Journal of Solids and Structures 38 (2001) 1641–1655.

[18] K. M. Liew, K. C. Hung, K. M. Lim, A solution method for analysis of cracked plates under vibration., Engineering fracture mechanics 48 (3) (1994) 393–404.

[19] T. Y. Ng, K. Y. Lam, K. M. Liew, Effect of FGM materials on parametric response of plate structures, Computer Methods in Applied Mechanics and Engineering 190 (2000) 953–962.

[20] J. Yang, H. S. Shen, Dynamic response of initially stressed functionally graded rectangular thin plates, Composite Structures 54 (2001) 497–508.

[21] H. Matsunaga, Free vibration and stability of functionally graded plates according to a 2D higher-order deformation theory, Composite Structures 82 (2008) 499–512.

[22] S. S. Vel, R. C. Batra, Exact solutions for thermoelastic deformations of functionally graded thick rectangular plates, AIAA J 40 (2002) 1421–1433.

[23] S. S. Vel, R. C. Batra, Three-dimensional exact solution for the vibration of functionally graded rectangular plates, Journal of Sound and Vibration 272 (2004) 703–730.

[24] V. Birman, Buckling of functionally graded hybrid composite plates, in: Proceedings of 10th Conference on Engineering Mechanics, Vol. 2, 1995, pp. 1199–1202.

[25] R. Javaheri, M. Eslami, Buckling of functionally graded plates under in-plane compressive loading, ZAMM 82 (2002) 277–283.

[26] J. Woo, S. Meguid, K. Liew, Thermomechanical postbuckling analysis of functionally graded plates and shallow cylindrical shells, Acta Mech. 165 (2003) 99–115.

[27] T. Prakash, M. Ganapathi, Supersonic flutter characteristics of functionally graded flat panels including thermal effects, Composite Structures 72 (2006) 10–18.

[28] H. Haddadpour, H. Navazi, F. Shadmehri, Nonlinear oscillations of a fluttering functionally graded plate, Composite Structures 79 (2007) 242–250.

[29] K.-J. Sohn, J.-H. Kim, Structural stability of functionally graded panels subjected to aero-thermal loads, Composite Structures 82 (2008) 317–325.

[30] K.-J. Sohn, J. Kim, Nonlinear thermal flutter of functionally graded panels under a supersonic flow, Composite Structures 88 (2009) 380–387.

[31] J. Yang, Y. Hao, W. Zhang, S. Kitipornchai, Nonlinear dynamic response of a functionally graded plate with a through-width surface crack, Nonlinear Dynamics 59 (2010) 207–219.

[32] S. Kitipornchai, L. Ke, J. Y. andY Xiang, Nonlinear vibration of edge cracked functionally graded Timoshenko beams, Journal of Sound and Vibration 324 (2009) 962–982.

[33] S. Natarajan, P. Baiz, M. Ganapathi, P. Kerfriden, S. Bordas, Linear free flexural vibration of cracked functionally graded plates in thermal environment, Computers and Structures 89 (2011) 1535–1546.

[34] S. Natarajan, P. Baiz, S. Bordas, P. Kerfriden, T. Rabczuk, Natural frequencies of cracked functionally graded material plates by the extended finite element method, Composite Structures 93 (2011) 3082–3092.

[35] P. M. Baiz, S. Natarajan, S. Bordas, P. Kerfriden, T. Rabczuk, Linear buckling analysis of cracked plates by SFEM and XFEM, Journal of Mechanics of Materials and Structure 6 (2011) 1213–1238.

[36] L. B. a. da Veiga, A. Buffa, C. Lovadina, M. Martinelli, G. Sangalli, An iso-geometric method for the reissner-mindlin plate bending problem, Computer Methods in Applied Mechanics and Engineering 209–212 (2012) 45–53.

[37] W. Kanok-Nukulchai, W. Barry, K. Saran-Yasontorn, P. Bouillard, On elimination of shear locking in the element-free galerkin method, International Journal for Numerical Methods in Engineering 52 (2001) 705–725.

[38] F. Kikuchi, K. Ishii, An improved 4-node quadrilateral plate bending element of the reissne-mindlin type, Computational Mechanics 23 (1999) 240–249.

[39] L. Wu, Thermal buckling of a simply supported moderately thick rectangular FGM plate, Composite Structures 64 (2004) 211–218.

[40] S. Rajasekaran, D. Murray, Incremental finite element matrices, ASCE Journal of Structural Divison 99 (1973) 2423–2438.

[41] V. Birman, L. Librescu, Supersonic flutter of shear deformation laminated flat panel, Journal of Sound and Vibration 139 (1990) 265–275.

[42] M. Ganapathi, M. Touratier, Supersonic flutter analysis of thermally stressed laminated composite flat panels, Composite Structures 34 (1996) 241–248.

[43] J. A. Cottrell, T. J. Hughes, Y. Bazilevs, Isogeometric analysis: Toward integration of CAD and FEA, John Wiley, 2009.

[44] V. P. Nguyen, R. N. Simpson, S. P. Bordas, T. Rabczuk, An introduction to Isogeometric analysis with MATLAB implementation: FEM and XFEM formulations, in review.

[45] M. Singha, T. Prakash, M. Ganapathi, Finite element analysis of functionally graded plates under transverse load, Finite elements in Analysis and Design 47 (2011) 453–460.

[46] D. Gilhooley, R. Batra, J. Xiao, M. McCarthy, J. Gillespie, Analysis of thick functionally graded plates by using higher order shear and normal deformable plate theory and MLPG method with radial basis functions, Composite Structures 80 (2007) 539–552.

[47] Y. Lee, X. Zhao, K. Liew, Thermo-elastic analysis of functionally graded plates using the element free $kp-$Ritz method, Smart Materials and Structures 18 (2009) 035007.

[48] H. Nguyen-Xuan, L. V. Tran, H. Thai, T. Nguyen-Thoi, Analysis of functionally graded plates by an efficient finite element method with node-based strain smoothing, Thin Walled Structures 54 (2012) 1–18.

[49] C. Thai, H. Nguyen-Xuan, N. Nguyen-Thanh, T.-H. Le, T. Nguyen-Thoi, T. Rabczuk, Static, free vibration and buckling analysis of laminated composite Reissner-Mindlin plates using NURBS based isogeometric approach, International Journal for Numerical Methods in Engineering 91 (2012) 571–603.

[50] L. Croce, P. Venini, Finite elements for functionally graded Reissner-Mindlin plates, Computer Methods in Applied Mechanics and Engineering 193 (2007) 705–725.

[51] X. Zhao, K. Liew, Geometrically nonlinear analysis of functionally graded plates using the element free $kp-$Ritz method, Computer Methods in Applied Mechanics and Engineering 198 (2009) 2796–2811.

[52] H. Nguyen-Xuan, L. V. Tran, T. Nguyen-Thoi, H. Vu-Do, Analysis of functionally graded plates using an edge-based smoothed finite element method, Composite Structures 93 (2011) 3019–3039.

[53] X. Zhao, Y. Lee, K. Liew, Free vibration analysis of functionally graded plates using the element free $kp-$Ritz method, Journal of Sound and Vibration 319 (2009) 918–939.

[54] S. H. Hashemi, M. Fadaee, S. Atashipour, A new exact analytical approach for free vibration of reissne-mindlin functionally graded rectangular plates, International Journal of Mechanical Sciences 53 (2011) 11–22.

[55] M. Ganapathi, T. Prakash, Thermal buckling of simply supported functionally graded skew plates, Composite Structures 74 (2006) 247–250.